POLITECNICO

MILANO 1863

SCUOLA DI INGEGNERIA INDUSTRIALE E DELL'INFORMAZIONE

Dipartimento di Scienze e Tecnologie Aerospaziali

MASTER THESIS IN AERONAUTICAL ENGINEERING

Large Eddy Simulation of the Transitional Flow around the SD7003 Airfoil and Application to Blade–Vortex Interaction

Relatore
Prof. Antonella Abbà

Candidato
Andrea Pio Catello Bresciani
Matr.898953

Ringraziamenti

Vorrei ringraziare la Professoressa Antonella Abbà (e i suoi consulenti sperimentali!) per il costante supporto, i preziosi consigli e l'infinita disponibilità in questi mesi. Le risorse di calcolo sono state messe a disposizione dal consorzio CINECA grazie ai progetti ISCRA-C PAVILES, ISCRA-C AVIPALES e ISCRA-B LESDY; la mia riconoscenza va alle persone che vi lavorano per il loro aiuto.

Un grandissimo grazie a tutti i miei amici e compagni di corso per aver condiviso con me questi anni al Politecnico, per averli resi più divertenti, meno stressanti e molto meno produttivi. Grazie a Riccardo, Tommaso, Andrea, Alessio[1], Roberto e Caterina. Un ringraziamento particolare a Matteo che, oltre ai meriti precedenti, ha anche quello di avermi sopportato in questi ultimi mesi, non farò mai nulla di sufficientemente *buonissimo* per sdebitarmi.

I ringraziamenti più importanti vanno alla mia famiglia che mi ha supportato in tutti questi anni di studio e a Sara che è sempre stata al mio fianco con infinita pazienza e affetto. Non solo questa tesi, ma tutti questi anni non sarebbero stati possibili senza il vostro aiuto. Grazie, davvero.

---

[1] Lello

Sommario

In questa tesi è stata studiata la corrente transizionale attorno al profilo SD7003 a $\alpha = 8°$, $Re = 60\,000$ e $Ma = 0.2$ utilizzando le *Large Eddy Simulations* con l'adattività polinomiale in una discretizzazione con elementi finiti discontinui di Galerkin. Questo è un *test case* particolarmente impegnativo poiché è presente una bolla di separazione laminare con transizione e riattacco dello strato limite turbolento. Inoltre le dimensioni della bolla sono fortemente influenzate dalla transizione. I risultati ottenuti col modello dinamico anisotropo sono stati confrontati con quelli ottenuti con un modello implicito, misure sperimentali e altri risultati numerici disponibili in letteratura. L'adattività polinomiale ha confermato la sua capacità di rappresentare correttamente la corrente con un grande risparmio del costo computazionale. Inoltre i risultati ottenuti col modello anisotropo si avvicinano alle misure sperimentali grazie alla capacità di tale modello di cogliere il *backscatter* di energia dalle scale di sotto-griglia. A partire dal campo di moto statisticamente stazionario ottenuto, è stata studiata l'interazione viscosa, parallela tra vortice e profilo nello stesso contesto numerico. Questa interazione è presente in molti problemi ingegneristici: il campo di applicazione più vicino a questo lavoro è nel progetto di *micro aerial vehicles* per via del basso numero di Reynolds scelto. Un vortice modellato è stato sovrapposto alla corrente attorno al profilo SD7003 e l'adattività polinomiale dinamica è stata utilizzata con successo per seguire il trasporto del vortice nel tempo. I carichi aerodinamici sono stati confrontati con quelli ottenuti con una simulazione senza vortice. A differenza del coefficiente di resistenza che torna rapidamente alla condizione statisticamente stazionaria, i transitori per i coefficienti di portanza e momento sono più lunghi a causa dell'effetto del vortice sulla bolla di separazione laminare.

Parole chiave: Large Eddy Simulation, Discontinuous Galerkin, adattività polinomiale, SD7003, bolla di separazione laminare, modello di sotto-griglia, interazione vortice-profilo

Abstract

In this thesis the transitional flow around the SD7003 airfoil at $\alpha = 8°$, $Re = 60\,000$ and $Ma = 0.2$ was investigated employing p-adaptive large eddy simulations in a Discontinuous Galerkin framework. This test case is particularly challenging since a *laminar separation bubble* (LSB) with transition and reattachment of the turbulent boundary layer (BL) has been observed. Furthermore the dimensions of the LSB are greatly affected by transition. The results obtained with the dynamic anisotropic model have been compared with the implicit model computations, experimental measurements and other numerical results available in literature. The polynomial adaptivity technique confirmed its capability to correctly represent the flow with a great saving in the computational cost. Furthermore the results obtained with the dynamic anisotropic model are close to experimental measurements thanks to the capability of this model to capture the energy backscatter from the subgrid scales. Starting from the statistically steady state flow field obtained, the viscous, parallel, blade-vortex interaction (BVI) has been studied in the same numerical framework. The BVI is a phenomenon of common occurrence in several engineering problems: because of the low Reynolds number chosen, the closest application field of the present work is in the design of micro aerial vehicles. A modelled vortex has been superimposed to the flow around the SD7003 airfoil and the *dynamic* p-adaptivity has been successfully employed to capture its advection over time. The loads have been recorded and compared with a reference simulation without the vortex. While the drag rapidly comes back to its steady-state value, the transients for lift and moment coefficients are longer because of the effect of the vortex on the LSB.

Keywords: Large Eddy Simulation, Discontinuous Galerkin, polynomial adaptivity, SD7003, Laminar Separation Bubble, subgrid model, Blade-Vortex Interaction

Contents

List of Figures

List of Tables

Chapter 1

Introduction

Computational fluid dynamics is today the main tool, together with experimental studies, to investigate turbulent flows. Such flows show a large range of time and length scales: the simulation should resolve all these scales to represent correctly the flow. The smallest time and length scales can be estimated, according to Kolmogorov theory, as $O(Re^{-3/4})$ and $O(Re^{-0.8})$ respectively. This means that they become smaller increasing the Reynolds number, which is extremely high in the majority of the aeronautical applications. Because of that, the computational cost required to solve all the turbulent scales is prohibitive for practical applications. However, this approach, called Direct Numerical Simulation (DNS), is employed for fundamental research in very simple geometries and at moderate Reynolds numbers. The results are considered as accurate as the one coming from experiments.

Today the most common way to tackle turbulent flows problems are the Reynolds average Navier–Stokes equations (RANS), thanks to the fact that only the mean (in time) flow quantities are solved and all the fluctuations in the smaller time and length scales are modelled. Lots of models have been suggested, the most common rely on the turbulent viscosity which can be obtained with algebraic or differential equations from turbulence quantities, such as the turbulent kinetic energy k or the dissipation rate of turbulent kinetic energy ε. RANS are used in industry and in research that involves complex geometries and high Reynolds number and the computational cost is orders of magnitude lower than a DNS. However the modelled part of the time and length scales leads to limited accuracy which is not always acceptable.

Between the representation of all the turbulence scales (DNS) and the modelling of all the turbulence effects (RANS), there is the Large Eddy Simulation (LES) approach. In this case the flow quantities are filtered in space rather than averaged in time. In this way only the largest eddies are fully represented (the one linked to the domain and time scales), while the smallest ones, which can be supposed to be universal, are modelled. The computational cost is midway between a RANS and a DNS computation, but nowadays still not feasible for a full scale aeronautic model. Here the LES approach has been used to model the statistically 2D flow around the Selig–Donovan (SD) 7003 airfoil at a moderate Reynolds number.

The flow around the SD7003 airfoil at $Re = 60\,000$ or $Re = 30\,000$ is a common

test case[1] to asses the accuracy of a RANS or LES implementation in the prediction of the transition to turbulence and reattachment. Indeed, also at low angle of attack, there is a laminar boundary layer separation with the transition in the shear layer. The reattachment of the turbulent boundary layer leads to the formation of a recirculating region called laminar separation bubble (LSB). This flow is particularly challenging to simulate numerically, since it shows a wide variety of turbulent scales: large scale vortices, which are formed in the recirculating region, breaks down into small scale structures while they are advected downstream.

Since the most common RANS models fail in low Reynolds conditions, ad hoc RANS turbulence models have been developed to correctly represent this flow; see for example the works of Catalano and Tognaccini (2010), Catalano and Tognaccini (2011) and Bernardos, Richez, Gleize, and Gerolymos (2019). The reference points for the assessment of these models are the LES of Catalano and Tognaccini (2009) and Galbraith and Visbal (2008); however several authors applied the LES approach to this flow to assess the accuracy of their particular LES implementation or discretisation technique: Bolemann et al. (2015), Bassi et al. (2016) and Uranga, Persson, Drela, and Peraire (2009) used the discontinuous Galerkin method; Boom and Zingg (2013) and Garmann, Visbal, and Orkwis (2013) used finite difference methods (Summation-by-parts and compact, respectively). More recently Qin, Koochesfahani, and Jaberi (2018) used this test case to study the effect of an harmonic variation in the free-stream angle of attack and velocity magnitude on the LSB; Sarlak (2017) studied the effect that the Reynolds number and the subgrid scale modelling have in this flow; finally Breuer (2018) compared the results obtained varying the inflow turbulence, similarly to what has been done experimentally by Herbst, Kähler, and Hain (2018). The $\mathbb{P}$-adaptive method has been applied very recently by Wang, Gobbert, and Yu (2019) (preprint, at the present time) to save computational resources without affecting the accuracy of the solution.

From an applicative point of view, the study of a low Reynolds flow around an airfoil is particularly interesting in the development Micro Aerial Vehicle (MAV). For this reason and to match the results of numerical simulation, this test case have been studied experimentally, for example, in the works of Burgmann and Schröder (2008), Ol, McAuliffe, Hanff, Scholz, and Kaehler (2005), Radespiel, Windte, and Scholz (2007), McAuliffe and Yaras (2005), Zhang, Hain, and Kähler (2008) and Hain, Kahler, and Radespiel (2009). More recently Herbst et al. (2018) analysed the effect of free stream turbulence on the LSB.

Another important problem in the design of a MAV is the interaction between the airfoil and a vortex, which can be generated either by the flapping motion or by a previous blade (tip vortex). This interaction is know as blade–vortex interaction (BVI) or airfoil–vortex interaction.

The interaction of vortices with solid bodies is a complex fluid dynamic phenomenon of common occurrence in a lot of engineering problems such as rotorcraft flows, heat exchangers, bridge pilings, offshore structures and flows around buildings. This interaction usually cause negative effects such as noise, unsteady aerodynamic loads and structural vibration. Both experimental and numerical approach have

---

[1]It has been proposed within the "International Workshop on High-Order CFD Methods".

been used to better understand the physics behind this phenomenon and to predict the most critical conditions. Particularly interesting from the aeronautic point of view is the BVI in the helicopter rotor where the tip vortex released by a blade interact with the one of the following blades. It is particularly challenging since it usually occur during slowly descending flight when the rotor wake remains in the close proximity of the rotor disk, causing highly unsteady and three dimensional flow field. However the BVI is usually classified in three different categories depending on the relative orientation between the vortex axis and the blade span:

- Parallel BVI occurs when the vortex and the blade axis are parallel;

- Perpendicular BVI occurs when the vortex and the blade axis are perpendicular and the vortex axis is aligned with the streamwise direction;

- Orthogonal BVI occurs when the vortex and the blade axis are perpendicular to each other and also to the streamwise direction.

In the most general case the vortex axis and the blade span are arbitrarily oriented and in literature it is usually referred as oblique BVI. This is the practical scenario, but the simplified classification allows to better comprehend the basic interactions that should be present in the real case. Nevertheless, in some regions of the blades, the interaction can be simplified with one of the previous models. The interaction can also be viscous or inviscid depending if the vortex hit directly the blade (viscous) or it passes in its close proximity (inviscid). An extensive review of the body–vortex interaction has been made by Rockwell (1998) and by Wilder and Telionis (1998) on parallel BVI in particular.

It is particularly challenging to investigate experimentally the parallel BVI, since it is not trivial to generate a single vortex. In a wind tunnel the vortex generator is usually an airfoil collocated upstream to the target airfoil. The upstream airfoil is moved with a pitch or plunge motion (or a combination of the two) to generate two vortices: one detaching from the leading edge (LEV) and one from the trailing edge (TEV). This configuration is known as *Schmidt–propeller configuration* and it was conceived to extract vortical energy from the upstream airfoil to generate thrust on the static airfoil (propeller). Measurement of parallel BVI in this configuration have been made for example by Wilder and Telionis (1998); Rival, Manejev, and Tropea (2010) and Peng and Gregory (2015).

Since in an experimental facility to study parallel BVI there are always a LEV and a TEV, the numerical approach is a powerful method to investigate the interaction between an airfoil and a single vortex. The parallel blade–vortex interaction has been studied with a RANS approach, coupled with a vorticity confinement method (see for example Steinhoff and Raviprakash (1995) and Morvant, Badcock, and Barakos (2005)) to prevent the an excessive diffusion of the advected vortex due to a poor resolution of the grid. Chimera method or overlapped grids approach have been also used in the same framework to predict BVI noise (Tanabe et al., 2007 and Tanabe, Saito, Takasaki, and Fujita, 2009).

A hybrid RANS/LES method to study the parallel BVI has been applied by Felten and Lund (2005), however the first fully LES of a parallel blade–vortex interaction has been made by Ilie, Nitzche, and Matida (2007) followed by Ilie

(2019), where a simplified aeroelastic model has been presented. The use of a LES approach not only guarantees a better accuracy of the solution, but, furthermore, it does not require any *ad hoc* technique to prevent the over-diffusion of the vortex.

In the present work the LES approach has been used to study the transitional flow around the SD7003 airfoil and to investigate the parallel interaction between a vortex and the airfoil. The numerical code is based on the *Discontinuous Galerkin* finite element method characterised by high order accuracy and very good scalability properties in High Performance Computing facilities. Furthermore the $\mathbb{P}$-adaptive method developed by Tugnoli (2017) and the dynamic anisotropic model developed by Abbà, Bonaventura, Nini, and Restelli (2015) have been assessed in this test case. The present work is part of a wider project in the *Dipartimento di Scienze e Tecnologie Aerospaziali* (Department of Aerospace Science and Technology) of *Politecnico di Milano* which aims to study BVI in rotorcraft flows. Perpendicular BVI has been investigated by Droandi, Gibertini, and Zanotti (2016) and ongoing experimental measurements are focused on parallel BVI.

In chapter 2 the numerical framework is explained. In chapter 3 the statistically steady state flow around the SD7003 airfoil is presented and it is compared with experimental data and other numerical results. Finally the BVI results are shown in the chapter 4.

Chapter 2

Fluid Dynamics Simulation Framework

In the present chapter the Large Eddy Simulation framework will be introduced starting from the compressible Navier–Stokes equations and filtering operator in section 2.1. In section 2.2 four subgrid models are explained: the ones adopted in the present work are the dynamic anisotropic model 2.2.3 and the implicit model 2.2.4. The discretisation and the polynomial adaptivity techniques are treated in sections 2.3 and 2.4 respectively. Finally the implementation details are explained in section 2.5. A more detailed explanation of all the topics treated in this chapter can be found in the works of Tugnoli (2017), Tugnoli, Abbà, Bonaventura, and Restelli, 2016, Abbà et al. (2015) and Abbà, Campaniello, and Nini (2017).

2.1 Governing Equations

The compressible Navier–Stokes equations, have been used to model a compressible viscous flow. The dimensional form, where each variable is denoted by superscript "d", reads:

$$\partial_{t^d}\rho^d + \partial_{x_j^d}(\rho^d u_j^d) = 0 \tag{2.1a}$$

$$\partial_{t^d}(\rho^d u_i^d) + \partial_{x_j^d}(\rho^d u_i^d u_j^d) + \partial_{x_i^d}p^d - \partial_{x_j^d}\sigma_{ij}^d = 0 \tag{2.1b}$$

$$\partial_{t^d}(\rho^d e^d) + \partial_{x_j^d}(\rho^d h^d u_j^d) - \partial_{x_j^d}(u_i^d \sigma_{ij}^d) + \partial_{x_j^d}q_j^d = 0 \tag{2.1c}$$

The equations (2.1) represent, respectively, the mass, momentum and total energy balance. The unknowns are the density ρ^d, the momentum density $\rho^d \mathbf{u}^d$, and the total energy density $\rho^d e^d$. The specific total energy e^d is defined as the sum of the specific internal energy e_i^d and the specific kinetic energy $\frac{1}{2}u_k^d u_k^d$:

$$e^d = e_i^d + \frac{1}{2}u_k^d u_k^d \tag{2.2}$$

h^d is the specific enthalpy, defined as $\rho^d h^d = \rho^d e^d + p^d$. The problem is closed with a polytropic ideal gas model, which provides the (two) state equations needed:

$$T^d = \frac{(\gamma - 1)}{R}e_i^d, \qquad P^d = (\gamma - 1)\rho^d e_i^d \tag{2.3}$$

Finally the constitutive equations for the heat flux $\mathbf{q}^d$ and for the viscous stress tensor σ_{ij}^d are required:

$$q_j^d = -\frac{\mu^d c_p}{Pr} \partial_{x_j^d} T^d, \qquad \sigma_{ij}^d = \mu^d S_{ij}^{\mathrm{d},d} \tag{2.4}$$

where $S_{ij}^{\mathrm{d},d} = S_{ij}^d - \frac{1}{3} S_{kk}^d \delta_{ij}$, $S_{ij}^d = \partial_{x_i^d} u_j^d + \partial_{x_j^d} u_i^d$ and $Pr = 0.72$ is the Prandtl number. The dynamic viscosity μ^d is assumed to depend only by the temperature with the power law

$$\mu^d \left(T^d \right) = \mu_0^d \left(\frac{T^d}{T_0^d} \right)^\alpha \tag{2.5}$$

with $\alpha = 0.7$, according to Sutherland hypothesis.

The dimensionless form of the compressible Navier–Stokes equations is obtained defining reference quantities (subscript "r") for all the variables such that:

$$\mathbf{x}^d = L_r \mathbf{x}, \quad t^d = t_r t, \quad \rho^d = \rho_r \rho, \quad \mathbf{u}^d = u_r \mathbf{u},$$
$$p^d = p_r p, \quad e^d = e_r e, \quad \mu^d = \mu_r \mu, \quad T^d = T_r T, \quad q^d = q_r q. \tag{2.6}$$

The variables without superscript nor subscript are the dimensionless ones. Only the quantities L_r, ρ_r, u_r and T_r are assumed, while all the other reference quantities are obtained as follows:

$$t_r = \frac{L_r}{u_r}, \quad p_r = \rho_r R T_r, \quad e_r = R T_r, \quad \mu_r = \mu_0^d \left(\frac{T_r}{T_0^d} \right)^\alpha, \quad q_r = \frac{\mu_r c_p T_r}{Pr\, L_r} \tag{2.7}$$

Using the equations (2.7), the Navier–Stokes equations can now be rewritten in non–dimensional form:

$$\partial_t \rho + \partial_j (\rho u_j) = 0 \tag{2.8a}$$

$$\partial_t (\rho u_i) + \partial_j (\rho u_i u_j) + \frac{1}{\gamma\, Ma^2} \partial_i p - \frac{1}{Re} \partial_j \sigma_{ij} = 0 \tag{2.8b}$$

$$\partial_t (\rho e) + \partial_j (\rho h u_j) - \frac{\gamma\, Ma^2}{Re} \partial_j (u_i \sigma_{ij}) + \frac{1}{k\, Re\, Pr} \partial_j q_j = 0 \tag{2.8c}$$

with $Ma = \dfrac{u_r}{\sqrt{\gamma R T_r}}$, $Re = \dfrac{\rho_r u_r L_r}{\mu_r}$, $\gamma = \dfrac{c_p}{c_v}$ and $k = \dfrac{R}{c_p}$. The dimensionless total energy e and the dimensionless enthalpy h are defined as

$$e = e_i + \frac{\gamma\, Ma^2}{2} u_k u_k, \qquad h = e + \frac{p}{\rho} \tag{2.9}$$

being e_i the dimensionless internal energy. The dimensionless constitutive equations for the heat flux q_j and the viscous stress tensor σ_{ij} are

$$q_j = -\mu \left(T \right) \partial_j T \qquad \sigma_{ij} = \mu \left(T \right) S_{ij}^{\mathrm{d}} \tag{2.10}$$

with the dynamic viscosity $\mu \left(T \right) = T^\alpha$ and $S_{ij}^{\mathrm{d}} = S_{ij} - \frac{1}{3} S_{kk} \delta_{ij}$, $S_{ij} = \partial_i u_j + \partial_j u_i$. Finally, the dimensionless state equations for a PIG reads

$$T = \frac{k}{1-k} e_i, \qquad p = \frac{k}{1-k} \rho e_i \tag{2.11}$$

2.1.1 Filtering

The idea behind the LES approach is filtering (rather than average) the Navier–Stokes equations (2.8). The filter operator is denoted by $\overline{\cdot}$ and it is characterised by the length scale $\overline{\Delta}$. The precise definition of the operator is linked to the discretisation used and it will be treated in section 2.3. The fundamental properties of a LES filter to allow an easier manipulation of Navier–Stokes equations are (1) conservation of constant, (2) linearity and (3) commutation with derivation. The last property is not verified in case of anisotropic or inhomogeneous filters, which is the case of this work as well as the majority of practical LES. However the extra term (called *commutation error*) arising from the anisotropy of the filter will be neglected, as always done in literature. An estimate of the commutation error for some simple filters has been computed by Sagaut and Meneveau (2006). In a discontinuous Galerkin discretisation (see section 2.3) the filter is uniform on the element, hence the commutation error is formally included in the error arising from the numerical fluxes.

As customary while manipulating the compressible Navier–Stokes equations, the Favre filtering operator $\widetilde{\cdot}$ is here introduced to avoid an extra subgrid term in the mass conservation equation:

$$\overline{\rho u_i} = \overline{\rho}\widetilde{u}_i, \quad \overline{\rho e} = \overline{\rho}\widetilde{e}, \quad \overline{\rho e_i} = \overline{\rho}\widetilde{e}_i, \quad \overline{\rho h} = \overline{\rho}\widetilde{h} = \overline{\rho}\widetilde{e} + \overline{p}. \tag{2.12}$$

The filtered Navier–Stokes equations can be obtained from equations (2.8); the resulting equations are:

$$\partial_t\overline{\rho} + \partial_j(\overline{\rho}\widetilde{u}_j) = 0 \tag{2.13a}$$

$$\partial_t(\overline{\rho}\widetilde{u}_i) + \partial_j(\overline{\rho}\widetilde{u}_i\widetilde{u}_j) + \frac{1}{\gamma\,Ma^2}\partial_i\overline{p} - \frac{1}{Re}\partial_j\widetilde{\sigma}_{ij}$$
$$= -\partial_j\tau_{ij} - \partial_j\epsilon_{ij}^{\text{sgs}} \tag{2.13b}$$

$$\partial_t(\overline{\rho}\widetilde{e}) + \partial_j(\overline{\rho}\widetilde{h}\widetilde{u}_j) - \frac{\gamma\,Ma^2}{Re}\partial_j(\widetilde{u}_i\widetilde{\sigma}_{ij}) + \frac{1}{k\,Re\,Pr}\partial_j\widetilde{q}_j$$
$$= -\partial_j(\rho h u_j)^{\text{sgs}} + \frac{\gamma\,Ma^2}{Re}\partial_j\phi_j^{\text{sgs}} - \frac{1}{k\,Re\,Pr}\partial_j\theta_j^{\text{sgs}} \tag{2.13c}$$

where

$$\tau_{ij} = \overline{\rho u_i u_j} - \overline{\rho}\widetilde{u}_i\widetilde{u}_j, \quad \epsilon^{\text{sgs}} = \overline{\sigma}_{ij} - \widetilde{\sigma}_{ij}, \quad (\rho h u_j)^{\text{sgs}} = \overline{(\rho h u_j)} - \overline{\rho}\widetilde{h}\widetilde{u}_j,$$
$$\phi_j^{\text{sgs}} = \overline{u_i\sigma_{ij}} - \widetilde{u}_i\widetilde{\sigma}_{ij}, \quad \theta_j^{\text{sgs}} = \overline{q}_j - \widetilde{q}_j \tag{2.14}$$

are the subgrid contributions. The filtered counter part of the constitutive equations (2.10) are simply:

$$\widetilde{q}_j = -\mu(\widetilde{T})\partial_j\widetilde{T} \qquad \widetilde{\sigma}_{ij} = \mu(\widetilde{T})\widetilde{S}_{ij}^d \tag{2.15}$$

with $\widetilde{S}_{ij}^{\text{d}} = \widetilde{S}_{ij} - \frac{1}{3}\widetilde{S}_{kk}\delta_{ij}$ and $\widetilde{S}_{ij} = \partial_i\widetilde{u}_j + \partial_j\widetilde{u}_i$. Finally the filtered state equations reads:

$$\widetilde{T} = \frac{k}{1-k}\widetilde{e}_i, \qquad \overline{p} = \frac{k}{1-k}\overline{\rho}\widetilde{e}_i \tag{2.16}$$

Note that $\overline{p} = \overline{\rho}\widetilde{T}$. From equation (2.9) the definitions of the filtered total energy $\widetilde{e}$ and the filtered enthalpy $\widetilde{h}$ can be obtained:

$$\overline{\rho}\widetilde{e} = \overline{\rho}\widetilde{e}_i + \frac{\gamma\,Ma^2}{2}(\overline{\rho}\widetilde{u}_k\widetilde{u}_k + \tau_{kk}), \qquad \overline{\rho}\widetilde{h} = \overline{\rho}\widetilde{e} + \overline{p} \qquad (2.17)$$

The subgrid contributions (2.14) represent the smaller, not resolved turbulent scales. Since they are not known a priori, they must be computed from the resolved (known) quantities through a turbulence model (see section 2.2). However some of them can be neglected: as suggested by Pino Martín, Piomelli, and Candler (2000) and Vreman, Geurts, and Kuerten (1995) and, supposing that $\overline{\sigma}_{ij} \approx \widetilde{\sigma}_{ij}$ and $\overline{q}_j \approx \widetilde{q}_i$, the terms $\partial_j \phi^{\mathrm{sgs}}$, ϵ^{sgs} and θ_j^{sgs} vanish. The term $(\rho h u_j)^{\mathrm{sgs}}$ can be rewritten in a more practical way: first of all combining the equations (2.17) and (2.16), the definition of the filtered enthalpy can be restated:

$$\begin{aligned}
\overline{\rho}\widetilde{h} &= \overline{\rho}\widetilde{e} + \overline{p} \\
&= \overline{\rho}\widetilde{e}_i + \frac{\gamma\,Ma^2}{2}(\overline{\rho}\widetilde{u}_k\widetilde{u}_k + \tau_{kk}) + \overline{\rho}\widetilde{T} \\
&= \frac{1}{k}\overline{\rho}\widetilde{T} + \frac{\gamma\,Ma^2}{2}(\overline{\rho}\widetilde{u}_k\widetilde{u}_k + \tau_{kk})
\end{aligned} \qquad (2.18)$$

Substituting the new definition (2.18) in the definition of $(\rho h u_j)^{\mathrm{sgs}}$ (2.14) and introducing the subgrid heat and turbulent diffusion fluxes

$$Q_i^{\mathrm{sgs}} = \overline{\rho u_i T} - \overline{\rho}\widetilde{u}_i\widetilde{T} = \overline{\rho}(\widetilde{u_i T} - \widetilde{u}_i\widetilde{T}) \qquad (2.19)$$
$$J_i^{\mathrm{sgs}} = \overline{\rho u_i u_k u_k} - \overline{\rho}\widetilde{u}_i\widetilde{u}_k\widetilde{u}_k = \overline{\rho}\widetilde{u_i u_k u_k} - \overline{\rho}\widetilde{u}_i\widetilde{u}_k\widetilde{u}_k \qquad (2.20)$$

one should obtain:

$$(\rho h u_i)^{\mathrm{sgs}} = \frac{1}{k}Q_i^{\mathrm{sgs}} + \frac{\gamma\,Ma^2}{2}(J_i^{\mathrm{sgs}} - \tau_{kk}\widetilde{u}_i) \qquad (2.21)$$

As suggested by Germano (1992) the subgrid turbulent diffusion flux J_i^{sgs} can be rewritten using the generalised central moments $\tau(u_i, u_j, u_k)$ as follows:

$$J_i^{\mathrm{sgs}} = \tau(u_i, u_k, u_k) + 2\widetilde{u}_k\tau_{ik} + \widetilde{u}_i\tau_{kk} \qquad (2.22)$$

being
$$\tau(u_i, u_j, u_k) = \overline{\rho}\widetilde{u_i u_j u_k} - \widetilde{u}_i\tau_{jk} - \widetilde{u}_k\tau_{ij} - \overline{\rho}\widetilde{u}_i\widetilde{u}_j\widetilde{u}_k \qquad (2.23)$$

Given the above definitions and assumptions the filtered Navier–Stokes equations (2.13) can be finally written as:

$$\partial_t\overline{\rho} + \partial_j(\overline{\rho}\widetilde{u}_j) = 0 \qquad (2.24\mathrm{a})$$

$$\partial_t(\overline{\rho}\widetilde{u}_i) + \partial_j(\overline{\rho}\widetilde{u}_i\widetilde{u}_j) + \frac{1}{\gamma\,Ma^2}\partial_i\overline{p} - \frac{1}{Re}\partial_j\widetilde{\sigma}_{ij}$$
$$= -\partial_j\tau_{ij} \qquad (2.24\mathrm{b})$$

$$\partial_t(\overline{\rho}\widetilde{e}) + \partial_j(\overline{\rho}\widetilde{h}\widetilde{u}_j) - \frac{\gamma\,Ma^2}{Re}\partial_j(\widetilde{u}_i\widetilde{\sigma}_{ij}) + \frac{1}{k\,Re\,Pr}\partial_j\widetilde{q}_j$$
$$= -\frac{1}{k}\partial_j Q_j^{\mathrm{sgs}} - \frac{\gamma\,Ma^2}{2}\partial_j(J_j^{\mathrm{sgs}} - \tau_{kk}\widetilde{u}_j) \qquad (2.24\mathrm{c})$$

2.2 Subgrid Models

The subgrid scale contributions must take into account all the effects arising from the not resolved scales which affect the resolved ones. If the cutoff frequency of the filter is (ideally) at the very end of the inertial subrange, the main effect that has to be modelled is the dissipation of the energy coming from the larger scale eddies. However the model should also allow the backscatter: even if globally the energy is transferred from the larger to the smaller scales, locally the energy could be transferred in the opposite way. This is a fundamental property for a model to avoid the over dissipation of the turbulent structures. As explained in section 2.2.1, the Smagorinsky model does not have this property, while it can be archived with the dynamic procedure (see section 2.2.2) proposed by Germano, Piomelli, Moin, and Cabot (1991). These two models are here explained for clarity and for a better comprehension of the model explained in section 2.2.3, but they will not be used.

The model adopted in the present work is the dynamic anisotropic model explained in section 2.2.3 and presented by Abbà, Cercignani, and Valdettaro (2003) for incompressible flows and extended to the compressible framework by Abbà et al. (2015). In this model the dynamic procedure is coupled with an anisotropic model to overcome the hypothesis that the principal directions of the subgrid stress tensor τ are aligned with the rate of strain tensor $\widetilde{S}_{ij}$.

2.2.1 Smagorinsky Model

The model, introduced by Smagorinsky (1963) and initially applied in weather forecast, is the most employed in LES context thanks to its simplicity. As the majority of RANS models, the deviatoric part of the subgrid stress tensor τ_{ij} is modelled through the single scalar value ν^{sgs} called turbulent viscosity:

$$\tau_{ij} - \frac{1}{3}\tau_{kk}\delta_{ij} = -\frac{1}{Re}\overline{\rho}\nu^{\text{sgs}}\widetilde{S}_{ij}^{d} \tag{2.25}$$

As pointed out by Pope (2000), this is a limitation for, mainly, two reasons. First of all, also in a simple flow as the one in an axisymmetric contraction (see the work of Uberoi (1956)), it is not true that the subgrid stress tensor depends only on the filtered (or mean, in RANS) strain rate S_{ij}, but a memory effect has been observed. Furthermore the subgrid stress tensor is not aligned with the strain rate tensor, which is implicitly assumed while saying that ν^{sgs} is a scalar value instead of a fourth order tensor. Because of the last assumption the turbulent viscosity models are also called isotropic models. As explained in section 2.2.3, the isotropic hypothesis can be removed developing an anisotropic model.

The effect of eq. (2.25) is to add a dissipation to the molecular one. In RANS models a complex relation between the turbulent viscosity and the averaged variables is required to take into account the effect of all the turbulent scales. On the contrary, in the LES approach, only the smallest turbulent scales are modelled and, thanks to Kolmogorov similarity theory, they can be supposed to be universal and to be modelled with the simple relation:

$$\nu^{\text{sgs}} = Re\, C_{S}^{2}\overline{\Delta}^{2}|\widetilde{S}| \tag{2.26}$$

where $C_S \simeq 0.1$ is the Smagorinsky constant (to be tuned, since it depends on the particular flow), $\overline{\Delta}$ is the characteristic length scale of the filter operator and $|\widetilde{S}|^2 = \frac{1}{2}\widetilde{S}_{ij}\widetilde{S}_{ij}$. [1]Despite the universality suggested by the Kolmogorov theory, a damping function f_D is required near the wall. The most used is the Van Driest damping function:

$$f_D = 1 - \exp\left(-y^+/A\right) \qquad (2.27)$$

with $A = 25$ and y^+ the dimensionless wall unit. So, the model (2.26) becomes:

$$\nu^{\text{sgs}} = Re\, C_S^2 \overline{\Delta}^2 |\widetilde{S}| f_D \qquad (2.28)$$

Since all the terms on the right-hand-side of equation (2.28) are positive, ν^{sgs} is always positive, hence no backscattering is possible. Furthermore, in case of laminar flow, the filter is still active, while it should be required $C_S = 0$, so that $\nu^{\text{sgs}} = 0$. For what concerns the isotropic part of the subgrid stress tensor, it could be neglected as usually done in the incompressible case (see for example the work of Erlebacher, Hussaini, Speziale, and Zang (1992)) or it can be modelled in a similar way of his deviatoric counterpart as done by Yoshizawa (1986) and Abbà et al. (2015):

$$\tau_{kk} = C_I \overline{\rho}\overline{\Delta}^2 |\widetilde{S}| \qquad (2.29)$$

The subgrid heat flux can be modelled as done by Eidson (1985) with the same viscosity coefficient:

$$Q_i^{\text{sgs}} = -\frac{Pr}{Pr^{\text{sgs}}}\overline{\rho}\nu^{\text{sgs}}\partial_i\widetilde{T}, \qquad (2.30)$$

The subgrid Prandtl number Pr^{sgs} is another constant which has to be tuned, usually $Pr^{\text{sgs}} \simeq Pr = 0.72$. Finally the term $\tau(u_i, u_j, u_k)$ can be neglected from J_i^{sgs}, hence the turbulent diffusion flux only depend on the subgrid stress tensor:

$$J_i^{\text{sgs}} \simeq 2\widetilde{u}_k\tau_{ik} + \widetilde{u}_i\tau_{kk} \qquad (2.31)$$

2.2.2 Smagorinsky Dynamic Model

To overcome the weaknesses of the Smagorinsky model, the dynamic procedure has been developed by Germano et al. (1991). The main idea is to allow C_S to vary inside the domain and in time: it is not set a priori but it is automatically computed at each time step and in each element of the domain. To do this, a second filtering operator (*test filter*) denoted by $\widehat{\cdot}$ with a characteristic length of $\widehat{\Delta}$ (usually $\widehat{\Delta} = 2\overline{\Delta}$) and the corresponding Favre filter $\breve{\cdot}$ have to be introduced as follows:

$$\widehat{\overline{\rho u_i}} = \widehat{\overline{\rho}}\breve{u}_i, \quad \widehat{\overline{\rho e}} = \widehat{\overline{\rho}}\breve{e}, \quad \widehat{\overline{\rho e_i}} = \widehat{\overline{\rho}}\breve{e}_i, \quad \widehat{\overline{\rho h}} = \widehat{\overline{\rho}}\breve{h} = \widehat{\overline{\rho}}\breve{e} + \widehat{\overline{p}}. \qquad (2.32)$$

Applying the filtering operator just introduced to the filtered momentum balance equation (2.24b) leads to:

$$\partial_t(\widehat{\overline{\rho}}\breve{u}_i) + \partial_j(\widehat{\overline{\rho}}\breve{u}_i\breve{u}_j) + \frac{1}{\gamma\, Ma^2}\partial_i\widehat{\overline{p}} - \frac{1}{Re}\partial_j\breve{\sigma}_{ij} = -\partial_j(\widehat{\tau}_{ij} + \mathcal{L}_{ij}) \qquad (2.33)$$

---

[1]If the filter length that tends to zero, also the turbulent viscosity tends to zero; hence the model is not active. Because of that it is usually said the LES tends to a DNS when reducing the resolution, while this is not true for a RANS.

where $\mathcal{L}_{ij}$ is the Leonard stress tensor defined as:

$$\mathcal{L}_{ij} = \widehat{\overline{\rho}\widetilde{u}_i\widetilde{u}_j} - \widehat{\overline{\rho}}\breve{\widehat{u}}_i\breve{\widehat{u}}_j. \tag{2.34}$$

Since the spatial scale of the test filter $\widehat{\cdot}$ is bigger than the one associated to $\overline{\cdot}$ [2], for the generic variable a, the following relation can be stated: $\widehat{\overline{a}} = \widehat{a}$. Because of that the eq. (2.33) reduces to:

$$\partial_t(\widehat{\overline{\rho}}\breve{\widehat{u}}_i) + \partial_j(\widehat{\overline{\rho}}\breve{\widehat{u}}_i\breve{u}_j) + \frac{1}{\gamma\,Ma^2}\partial_i\widehat{\overline{p}} - \frac{1}{Re}\partial_j\breve{\sigma}_{ij} = -\partial_j(\widehat{\tau}_{ij} + \mathcal{L}_{ij}). \tag{2.35}$$

It is worth noting that the Leonard stress tensor (2.34) is a known quantity as it can be computed applying the test filter to the variables $\overline{\rho}$ and $\widetilde{\mathbf{u}}$ which are the solutions of the filtered Navier–Stokes equations (2.24). It is assumed that the Smagorinsky model can be applied also to the deviatoric part of the term $\widehat{\tau}_{ij} + \mathcal{L}_{ij}$ of the equation (2.35) in the form

$$\widehat{\tau}_{ij}^d + \mathcal{L}_{ij}^d = -\widehat{\overline{\rho}}\widehat{\Delta}^2|\breve{\widetilde{S}}|C_S\breve{\widetilde{S}}_{ij}^d \tag{2.36}$$

as well as to τ_{ij}^d:

$$\tau_{ij}^d = -\overline{\rho}C_S\overline{\Delta}^2|\widetilde{S}|\widetilde{S}_{ij}^d \tag{2.37}$$

Substituting eq. (2.37) into eq. (2.36) leads to:

$$C_S\mathcal{R}_{ij} = \mathcal{L}_{ij}^d. \tag{2.38}$$

with $\mathcal{R}_{kl} = \widehat{\overline{\rho}\overline{\Delta}^2|\widetilde{S}|\widetilde{S}_{kl}^d} - \widehat{\overline{\rho}}\widehat{\Delta}^2|\breve{\widetilde{S}}|\breve{\widetilde{S}}_{kl}^d$. So, the value of C_S can be computed with a least square approach:

$$C_S = \frac{\mathcal{L}_{ij}^d\mathcal{R}_{ij}}{\mathcal{R}_{kl}\mathcal{R}_{kl}}. \tag{2.39}$$

Also the isotropic part of the subgrid stress tensor (modelled with eq. (2.29)) can be treated with a dynamic procedure, leading to:

$$C_I = \frac{\mathcal{L}_{kk}}{\widehat{\overline{\rho}}\widehat{\Delta}^2|\breve{\widetilde{S}}|^2 - \widehat{\overline{\rho}\overline{\Delta}^2|\widetilde{S}|^2}} \tag{2.40}$$

The subgrid heat flux can be modelled similarly:

$$Q_i^{\text{sgs}} = -\overline{\rho}\overline{\Delta}^2|\widetilde{S}|C_Q\partial_i\widetilde{T}, \tag{2.41}$$

and the coefficient C_Q can be computed dynamically:

$$C_Q = \frac{\mathcal{L}_i^Q\mathcal{R}_i^Q}{\mathcal{R}_k^Q\mathcal{R}_k^Q} \tag{2.42}$$

being $\mathcal{L}_i^Q = \widehat{\overline{\rho}\widetilde{u}_i\widetilde{T}} - \widehat{\overline{\rho}}\breve{\widehat{u}}_i\breve{\widetilde{T}}$ and $\mathcal{R}_i^Q = \widehat{\overline{\rho}\overline{\Delta}^2|\widetilde{S}|\partial_i\widetilde{T}} - \widehat{\overline{\rho}}\widehat{\Delta}^2|\breve{\widetilde{S}}|\partial_i\breve{\widetilde{T}}$. Following the work of Pino Martín et al. (2000) the third order generalised moment $\tau(u_i, u_j, u_k)$ from the turbulent diffusion flux J_i^{sgs} can be approximated as

$$\tau(u_i, u_k, u_k) = \widehat{\overline{\rho}\widetilde{u_iu_ku_k}} - \widehat{\overline{\rho}}\widetilde{u}_i\widetilde{u_ku_k} \tag{2.43}$$

---

[2]This is true also for as their Favre counterpart $\breve{\cdot}$ and $\widetilde{\cdot}$.

and modelled with the resolved kinetic energy gradient:

$$\tau(u_i, u_k, u_k) = -\overline{\rho}\overline{\Delta}^2 |\widetilde{S}| C_J \partial_i \left(\frac{1}{2} \widetilde{u}_k \widetilde{u}_k \right). \tag{2.44}$$

Finally, the coefficient C_J can be computed dynamically:

$$C_J = \frac{\mathcal{L}_i^J \mathcal{R}_i^J}{\mathcal{R}_k^J \mathcal{R}_k^J} \tag{2.45}$$

with $\mathcal{L}_i^J = \widehat{\overline{\rho}\widetilde{u}_i \widetilde{u}_k \widetilde{u}_k} - \widehat{\overline{\rho}}\breve{\widetilde{u}}_i \breve{\widetilde{u}}_k \breve{\widetilde{u}}_k$ and $\mathcal{R}_i^J = \widehat{\overline{\rho}\overline{\Delta}^2 |\widetilde{S}| \partial_i \left(\frac{1}{2} \widetilde{u}_k \widetilde{u}_k \right)} - \breve{\overline{\rho}}\widehat{\overline{\Delta}}^2 |\breve{\widetilde{S}}| \partial_i \left(\frac{1}{2} \breve{\widetilde{u}}_k \breve{\widetilde{u}}_k \right)$.

The dynamic procedure allows to overcome some the shortcomings of the Smagorinsky model: the model behaved very well near the wall and, hence, no damping function is required; furthermore the value of C_S is now zero in laminar flow condition and it can be negative to allow backscatter [3]. However, the Smagorinsky dynamic model is still limited by the isotropic assumption as his "static" counterpart. The coefficients, computed with the dynamic procedure, are very variable from point to point and, to avoid numerical instabilities, they are averaged over each element.

2.2.3   Dynamic Anisotropic Model

In this model the isotropic assumption is removed and the subgrid stress tensor is supposed proportional to the strain rate tensor through a fourth order symmetric tensor:

$$\tau_{ij} = -\overline{\rho}\overline{\Delta}^2 |\widetilde{S}| \mathcal{B}_{ijrs} \widetilde{S}_{rs} \tag{2.46}$$

A generic fourth order symmetric tensor can be represented as

$$\mathcal{B}_{ijrs} = \sum_{\alpha,\beta=1}^3 \mathcal{C}_{\alpha\beta} a_{i\alpha} a_{j\beta} a_{r\alpha} a_{s\beta} \tag{2.47}$$

with $\mathcal{C}_{\alpha\beta}$ a second order symmetric tensor and a_{ij} a rotation tensor. The eq. (2.47) is the generalisation for fourth order tensors of the diagonalisation of matrices. The choice of a_{ij} can be, in principle, arbitrary and several different choices have been analysed by Abbà, Cercignani, Picarella, and Valdettaro (2001), Abbà et al. (2003) and Gibertini, Abbà, Auteri, and Belan (2010); however the results do not appear to have strong dependency on the choice of the rotation tensor. For this reason, in the present work, as well as done by Abbà et al. (2015), the basis chosen is the canonic cartesian basis, i.e. $a_{ij} = \delta_{ij}$. Thanks to the simple rotation tensor chosen, the eq. (2.46) reduces to

$$\tau_{ij} = -\overline{\rho}\overline{\Delta}^2 |\widetilde{S}| \mathcal{C}_{ij} \widetilde{S}_{ij}, \tag{2.48}$$

where the repeated indices strands for a element by element multiplication, differently from the notation adopted until now. Similarly to what have been done in

---

[3]Actually, it is required to ensure to the total dissipation, resulting from the subgrid stresses and the viscous one, to be positive to avoid unphysical behaviour. See the work of Abbà et al., 2015 for the details.

section 2.2.2, the right hand side of eq. (2.35) has been modelled with (2.48) to develop the dynamic procedure. In this case the isotropic part of the term $\widehat{\tau}_{ij} + \mathcal{L}_{ij}$ has been treated together with the deviatoric one, leading to:

$$\widehat{\tau}_{ij} + \mathcal{L}_{ij} = -\widehat{\overline{\rho}}\widehat{\Delta}^2|\breve{\widetilde{S}}|\mathcal{C}_{ij}\breve{\widetilde{S}}_{ij}. \tag{2.49}$$

Substituting τ_{ij} from (2.48) in the above relation, the values for $\mathcal{C}_{ij}$ can be obtained:

$$\mathcal{C}_{ij} = \frac{\mathcal{L}_{ij}}{\widehat{\overline{\rho}\overline{\Delta}^2|\widetilde{S}|\widetilde{S}_{ij}} - \widehat{\overline{\rho}}\widehat{\Delta}^2|\widetilde{S}|\widetilde{S}_{ij}}. \tag{2.50}$$

The subgrid heat and turbulent diffusion fluxes are also modelled with a dynamic procedure and two second order tensors:

$$Q_i^{\text{sgs}} = -\overline{\rho}\overline{\Delta}^2|\widetilde{S}|\mathcal{B}_{ir}^Q\partial_r\widetilde{T} \tag{2.51}$$

$$\tau(u_i, u_k, u_k) = -\overline{\rho}\overline{\Delta}^2|\widetilde{S}|\mathcal{B}_{ir}^J\partial_r\left(\frac{1}{2}\widetilde{u}_k\widetilde{u}_k\right) \tag{2.52}$$

with

$$\mathcal{B}_{ir}^Q = \sum_{\alpha=1}^{3}\mathcal{C}_\alpha^Q a_{i\alpha}a_{r\alpha} \tag{2.53}$$

$$\mathcal{B}_{ir}^J = \sum_{\alpha=1}^{3}\mathcal{C}_\alpha^J a_{i\alpha}a_{r\alpha}. \tag{2.54}$$

Exploiting again the relation $a_{ij} = \delta_{ij}$, the following relations are obtained:

$$Q_i^{\text{sgs}} = -\overline{\rho}\overline{\Delta}^2|\widetilde{S}|\mathcal{C}_i^Q\partial_i\widetilde{T} \tag{2.55}$$

$$\tau(u_i, u_k, u_k) = -\overline{\rho}\overline{\Delta}^2|\widetilde{S}|\mathcal{C}_i^J\partial_i\left(\frac{1}{2}\widetilde{u}_k\widetilde{u}_k\right), \tag{2.56}$$

and the coefficients $\mathcal{C}_i^Q$ and $\mathcal{C}_i^J$ are computed with the dynamic procedure:

$$\mathcal{C}_i^Q = \frac{\mathcal{L}_i^Q}{\left(\widehat{\overline{\rho}\overline{\Delta}^2|\widetilde{S}|\partial_i\widetilde{T}} - \widehat{\overline{\rho}}\widehat{\Delta}^2|\breve{\widetilde{S}}|\partial_i\breve{\widetilde{T}}\right)} \tag{2.57}$$

$$\mathcal{C}_i^J = \frac{\mathcal{L}_i^J}{\left(\widehat{\overline{\rho}\overline{\Delta}^2|\widetilde{S}|\partial_i\left(\frac{1}{2}\widetilde{u}_k\widetilde{u}_k\right)} - \widehat{\overline{\rho}}\widehat{\Delta}^2|\breve{\widetilde{S}}|\partial_i\left(\frac{1}{2}\breve{\widetilde{u}}_k\breve{\widetilde{u}}_k\right)\right)}. \tag{2.58}$$

As done previously for the isotropic (Smagorinsky) dynamic model 2.2.2, the coefficients are averaged over the element to avoid numerical instabilities.

2.2.4 Implicit LES

As explained by Sagaut and Meneveau (2006), the Implicit LES (ILES) approach is based on the hypothesis that the effect of the subgrid scales on the resolved ones

is purely dissipative. This kind of simulation uses the dissipation introduced by the numerical upwind schemes or an explicit artificial dissipation term to model the subgrid dissipation: hence, the subgrid terms arising from the filtering operation are simply dropped. The amount of dissipation introduced depends both on the local resolution and on the numerical scheme adopted. Because of the purely dissipative nature of this approach, the ILES simulations are not able to capture the backscatter phenomenon.

2.3   Local Discontinuous Galerkin Discretisation

The equations (2.24) are discretised over the domain Ω through the so called Discontinuous Galerkin (DG) method. It was first introduced by Reed and Hill (1973) for steady state hyperbolic equations and, then, developed by Bassi and Rebay (1997) for parabolic problem in the following form. The domain is divided into elements K in which a space of basis function is defined. Differently from the finite element method, the continuity of the basis functions between each element is not prescribed. The Navier–Stokes equations (2.24) are rewritten in the following form:

$$\partial_t \mathbf{U} + \nabla \cdot \mathbf{F}^{\mathrm{c}}(\mathbf{U}) = \nabla \cdot \mathbf{F}^{\mathrm{v}}(\mathbf{U}, \nabla \mathbf{U}) - \nabla \cdot \mathbf{F}^{\mathrm{sgs}}(\mathbf{U}, \nabla \mathbf{U}) \qquad (2.59)$$

where $\mathbf{U} = [\overline{\rho}, \overline{\rho}\widetilde{\mathbf{u}}^T, \overline{\rho}\widetilde{e}]^T$ are the prognostic variables and the fluxes are divided into convective fluxes

$$\mathbf{F}^{\mathrm{c}} = \begin{bmatrix} \overline{\rho}\widetilde{\mathbf{u}} \\ \overline{\rho}\widetilde{\mathbf{u}} \otimes \widetilde{\mathbf{u}} + \frac{1}{\gamma Ma^2}\overline{p}\mathcal{I} \\ \overline{\rho}\widetilde{h}\widetilde{\mathbf{u}} \end{bmatrix}, \qquad (2.60)$$

viscous fluxes

$$\mathbf{F}^{\mathrm{v}} = \begin{bmatrix} 0 \\ \frac{1}{Re}\widetilde{\sigma} \\ \frac{\gamma Ma^2}{Re}\widetilde{\mathbf{u}}^T\widetilde{\sigma} - \frac{1}{k\,Re\,Pr}\widetilde{\mathbf{q}} \end{bmatrix}, \qquad (2.61)$$

and subgrid fluxes

$$\mathbf{F}^{\mathrm{sgs}} = \begin{bmatrix} 0 \\ \tau \\ \frac{1}{k}\mathbf{Q}^{\mathrm{sgs}} + \frac{\gamma Ma^2}{2}\left(\mathbf{J}^{\mathrm{sgs}} - \tau_{kk}\widetilde{\mathbf{u}}\right) \end{bmatrix}. \qquad (2.62)$$

In the present framework Cockburn and Shu (1998) introduced the so called Local Discontinuous Galerkin (LDG) method which is a generalisation of the DG method introduced by Bassi and Rebay (1997) and it is the one adopted in the present work. The second order system (2.59) is rewritten as a first order system, introducing the auxiliary variable $\mathcal{G}$ to indicate the gradient of $\varphi = [\widetilde{\mathbf{u}}^T, \widetilde{T}]^T$:

$$\partial_t \mathbf{U} + \nabla \cdot \mathbf{F}^{\mathrm{c}}(\mathbf{U}) = \nabla \cdot \mathbf{F}^{\mathrm{v}}(\mathbf{U}, \mathcal{G}) - \nabla \cdot \mathbf{F}^{\mathrm{sgs}}(\mathbf{U}, \mathcal{G}) \qquad (2.63a)$$

$$\mathcal{G} - \nabla \varphi = 0. \qquad (2.63b)$$

The discontinuous finite element space $\mathcal{V}_h$ is defined over a tetrahedral tessellation $\mathcal{T}_h$ of the domain Ω:

$$\mathcal{V}_h = \left\{ \mathcal{V}_h \in L^2(\Omega) : v_h|_K \in \mathbb{P}^{q_K}(K), \forall K \in \mathcal{T}_h \right\}, \qquad (2.64)$$

where $\mathbb{P}^{q_K}(K)$ is the space of polynomial functions of degree q_K in the element K. The numerical solution is searched in the space $\mathcal{V}_h$: $(\mathbf{U}_h, \mathcal{G}_h) \in ((\mathcal{V}_h)^5, (\mathcal{V}_h)^{4\times3})$ through the weak form of (2.63):

$$\forall K \in \mathcal{T}_h, \quad \forall v_h \in \mathcal{V}_h, \quad \forall \mathbf{r}_h \in \mathcal{V}_h^3$$

$$\frac{d}{dt}\int_K \mathbf{U}_h v_h \, d\mathbf{x} - \int_K \mathbf{F}(\mathbf{U}_h, \mathcal{G}_h) \cdot \nabla v_h \, d\mathbf{x} + \int_{\partial K} \widehat{\mathbf{F}}(\mathbf{U}_h, \mathcal{G}_h) \cdot \mathbf{n}_{\partial K} v_h \, d\sigma = 0 \quad (2.65a)$$

$$\int_K \mathcal{G}_h \cdot \mathbf{r}_h \, d\mathbf{x} + \int_K \varphi_h \nabla \cdot \mathbf{r}_h \, d\mathbf{x} - \int_{\partial K} \widehat{\varphi} \, \mathbf{n}_{\partial K} \cdot \mathbf{r}_h \, d\sigma = 0, \quad (2.65b)$$

where $\mathbf{F} = \mathbf{F}^c + \mathbf{F}^v + \mathbf{F}^{sgs}$ and the symbol $\widehat{\cdot}$ is used to indicate the numerical fluxes at the elements boundaries. The numerical fluxes employed are the Rusanov flux for the convective flux (2.66) and centred fluxes for the remaining fluxes (eqs. (2.67) to (2.69)):

$$\widehat{\mathbf{F}^c} = \frac{1}{2}[\mathbf{F}^c_L + \mathbf{F}^c_R + |\lambda|(\mathbf{U}_L \mathbf{n}_{\partial K,L} + \mathbf{U}_R \mathbf{n}_{\partial K,R})] \quad (2.66)$$

$$\widehat{\mathbf{F}^v} = \frac{1}{2}(\mathbf{F}^v_L + \mathbf{F}^v_R) \quad (2.67)$$

$$\widehat{\mathbf{F}^{sgs}} = \frac{1}{2}(\mathbf{F}^{sgs}_L + \mathbf{F}^{sgs}_R) \quad (2.68)$$

$$\widehat{\varphi} = \frac{1}{2}(\varphi_L + \varphi_R). \quad (2.69)$$

Following the modal DG formulation, the prognostic variables are represented in each element K with a orthogonal polynomial basis. Hence the generic numerical approximation a_h of the variable a can be written as:

$$a_h|_K = \sum_{l=0}^{n_\phi(K)} a^{(l)} \phi_l^K \quad (2.70)$$

where ϕ_l^K are the basis functions on the element K and $a^{(l)}$ are the modal coefficients of the $n_\phi + 1$ basis functions. To span the polynomial space $\mathbb{P}^{q_K}(K)$ of degree q_K in $\mathbb{R}^3$ the number of basis functions required is

$$n_\phi + 1 = \frac{1}{6}(q_K + 1)(q_K + 2)(q_K + 3). \quad (2.71)$$

The filtering operator introduced in section 2.1.1 can now be defined more precisely. In practical LES the application of the filter is purely formal since it is coincides with the discretisation of the equations: the filtering operator is the projector $\Pi_{\mathcal{V}_h} : L^2(\Omega) \to \mathcal{V}_h$ defined by:

$$\int_\Omega \Pi_{\mathcal{V}_h} uv \, d\mathbf{x} = \int_\Omega uv \, d\mathbf{x} \qquad \forall u, v \in \mathcal{V}_h. \quad (2.72)$$

Hence, the filtered counterpart of the generic variable a is simply:

$$\bar{a} = \Pi_{\mathcal{V}_h} a \, . \quad (2.73)$$

The test filter can be defined in a similar way using the subspace

$$\widehat{\mathcal{V}_h} = \left\{ \widehat{\mathcal{V}_h} \in L^2(\Omega) : \widehat{v_h}|_K \in \mathbb{P}^{\widehat{q_K}}(K), \forall K \in \mathcal{T}_h \right\} \tag{2.74}$$

with $0 \le \widehat{q_K} \le q_K$, so that $\widehat{a} = \Pi_{\widehat{\mathcal{V}_h}} a$.

Finally, the filter characteristic dimension used in the subgrid models is

$$\Delta(K) = \sqrt[3]{\frac{\text{Vol}(K)}{n_\phi + 1}}, \tag{2.75}$$

with $\text{Vol}(K)$ the volume of the element K.

Concerning the time discretisation, the solution is advanced with an explicit fourth order five stages Runge–Kutta method with a fixed time step.

2.4 Polynomial Adaptivity

The polynomial adaptivity technique consist in varying locally the degree of the polynomial approximation of the solution. The basic procedure is the following:

1. First of all, an indicator is computed in each element of the domain with the solution available at the current time step;

2. On the base of the value of the indicator and the chosen values of the thresholds, the polynomial degree of the solution in each element is increased, decreased or kept equal to the previous one;

3. Finally the solution is projected on the new base: in case of a decreasing of the polynomial degree, the high order contribution are simply truncated; in case of a increasing of the polynomial degree, the new contributions are initialised to zero.

In literature three main categories of p-adaptivity can be found. The first one is a truncation-error-based or discretisation-error-based adaptation (see for example the work of Kompenhans, Rubio, Ferrer, and Valero (2016) and Naddei (2019)), which usually uses as indicator an estimate of the truncation or discretisation error from the solution on a coarser grid or a lower degree approximation. In particular Naddei, de la Llave Plata, and Couaillier (2018) compared several discretisation-error-based indicators. The second one is an adjoint-based adaptation (see, for example, Bassi et al., 2019) which uses the adjoint solution and the residual, computed with the coarse space and injected in the fine space, to compute the indicator. This method can be useful if the user is interested in output functionals, such as lift or drag. However the additional cost can be large in case of unsteady turbulent simulations. The third category is a feature-based adaption and it is the one adopted in the present work as well as, for example, in the works of Tugnoli et al. (2016), Abbà, Bonaventura, Recanati, and Tugnoli (2019) and Wang et al. (2019). They are easy to implement and they rely on indicators based on some physical quantities of the flow field.

In the present work the indicator chosen is based on the second order structure function (SF)

$$D_{ij} = \langle [u_i(\mathbf{x} + \mathbf{r}, t) - u_i(\mathbf{x}, t)] [u_j(\mathbf{x} + \mathbf{r}, t) - u_j(\mathbf{x}, t)] \rangle \qquad (2.76)$$

where $\langle \cdot \rangle$ indicates the expected value operator. The SF gives a physical insight into the local flow condition: it represents the lack of correlation of the velocity between the two points $\mathbf{x}$ and $\mathbf{x} + \mathbf{r}$. Large values of the SF indicates that the velocity in the two points are poorly correlated and, hence, a higher resolution is necessary; on the contrary a very low value of the SF indicates that the velocities correlate well and, hence, the polynomial degree could be lowered.

Since the subgrid models performed well in case of homogeneous isotropic turbulence, the isotropic part of the SF has been subtracted from the indicator. After choosing two points in the element K, the indicator is computed as:

$$Ind_{SF}(K) = \sqrt{\sum_{ij} \left(D_{ij} - D_{ij}^{\mathrm{iso}} \right)^2}. \qquad (2.77)$$

To eliminate the arbitrariness of the two points $\mathbf{x}$ and $\mathbf{x} + \mathbf{r}$, the (2.77) is computed for the each couple of element vertices and then averaged.

In case of statistically stationary flow the polynomial adaptivity can be performed only once (*static adaption*): the indicator is computed on a converged uniform degree simulation every $\Delta t_{\mathrm{ind}} \geq \Delta t$, averaged for a time long enough to eliminate the time dependency and, finally, the resolution is adapted. The polynomial degree in each element is chosen on the base of the value of the indicator and on the values of the thresholds decided a priori. For example, if three different polynomial degrees q_1, q_2 and q_3 (with $q_1 < q_2 < q_3$) are used, two different thresholds ϵ_1 and ϵ_2 have to be chosen (with $\epsilon_1 < \epsilon_2$). The degree of the polynomial approximation is set as follows: if $Ind_{SF}(K) < \epsilon_1 < \epsilon_2$, the order is q_1; if $\epsilon_1 < Ind_{SF}(K) < \epsilon_2$, the order is q_2; if $\epsilon_1 < \epsilon_2 < Ind_{SF}(K)$, the order is q_3. The computational cost is reduced thanks to the fact that the indicator can be computed using an under resolved simulation without affecting the accuracy of the final adapted flow field (see Tugnoli, 2017 and Tugnoli et al., 2016). With the new polynomial degree distribution the mesh can be repartitioned to rebalance the computational load of the processors. This is done assigning a weight to each element of the mesh equal to the number of basis function required by the local polynomial degree. The simulation is finally resumed with the new polynomial degree distribution.

If the statistics of the flow field are unsteady a *dynamic adaption* of the polynomial degree is preferable to better represent the phenomenon. The indicator is computed every $\Delta t_{\mathrm{ind}} \geq \Delta t$ and the resolution is adapted every $\Delta t_{\mathrm{adapt}} \geq \Delta t_{\mathrm{ind}}$. In the present implementation, despite a possible huge change in the value of the indicator, the order in each element is decreased or increased only 1 per Δt_{adapt}; this is done to avoid too fast changes in the local resolution. The computational load rebalancing can be performed every $\Delta t_{reb} \geq \Delta t_{adapt}$, however the runtime mesh repartition has been not implemented yet. In case of dynamic adaption, the reduction of the computational cost is clear: the high polynomial degree is used only where (and when) necessary, without affecting the accuracy of the solution

(see again Tugnoli, 2017 and Abbà et al. (2019)). It should be noted that the dynamic adaption could be used also for statistically steady flow (see Wang et al., 2019). However, the downside is an increase of the computational cost due to the computation of the indicator and to the disequilibrium of the computational load of the processors (in case of no dynamic rebalancing). Hence, for steady simulations, the static adaption is preferable.

The choice of the thresholds is not trivial because there is not a rigorous way to set them. What it is usually done is changing the values of the threshold to obtain a total number of degrees of freedom comparable with the one that would be obtained with a uniform polynomial order intermediate between the ones used. Furthermore one should try to avoid to have, in two adjacent elements, a jump in the polynomial degree of two or more to avoid numerical instabilities and an excessive grid anisotropy (see Naddei, 2019).

2.5 Numerical Implementation

The numerical implementation is based on the open source `FEMilaro` finite element toolkit developed by Restelli (2017) and it is built in the solver `dg-comp`. It is written in the latest standard Fortran (2015) and it makes an extensive use of the object oriented paradigms. The mesh is generated with Gmsh and partitioned with the METIS library developed by Karypis and Kumar (1998). The parallelisation is obtained through a pure MPI framework.

The computational resources have been made available by the CINECA HPC facility on the MARCONI A2 partition thanks to the projects ISCRA-C PAVILES, ISCRA-C AVIPALES and ISCRA-B LESDY.

Chapter 3

SD7003 Test Case

The statistically stationary flow around the SD7003 airfoil at an angle of attack of $\alpha = 8°$, $Re = 60\,000$ and $Ma = 0.2$ has been considered. The Mach number chosen is sufficiently low to allow a meaningful comparison with the incompressible results available in literature, but high enough to avoid too small time steps required by the explicit time solver.

The main flow feature is an unsteady laminar separation bubble (LSB) on the suction side of the airfoil. The transition to turbulence takes place in free shear layer and it is triggered by a Kelvin–Helmholtz (KH) instability as observed by McAuliffe and Yaras (2005) and Burgmann and Schröder (2008). The reattachment point moves on the airfoil because of the shed of the vortices from the main recirculating region. The vortices are advected downstream and breaks down into small scale structures.

In section 3.1 the grids adopted, the boundary conditions and the statistics required are explained. A resolution sensibility analysis with the dynamic anisotropic model (see section 2.2.3) is presented in section 3.2. After that the Implicit LES (ILES) outcomes are shown in section 3.3. Finally, in section 3.4, the most significant results of the previous sections are discussed and compared with other numerical solutions and experimental measurements available in literature. The conclusions of the present chapter are summarised in section 3.5.

3.1   Simulation Set-Up

3.1.1   Computational Domain and Grids

The computational domain has the typical C-grid shape used for airfoil analysis (see fig. 3.1). The chord c of the airfoil is unitary. The trailing edge is located in $(0, 1c)$ and the airfoil is rotated by $8°$ around this point. The inflow boundary is a semicircumference of radius $5c$ centred in the origin. The outflow boundary is $10c$ downstream the airfoil. The thickness in the span-wise direction is $0.2c$, as always done in literature (see e.g. Bassi et al., 2016 or Boom and Zingg, 2013).

Two meshes have been used: the coarser mesh is composed by $57\,479$ tetrahedra and the more refined one by $110\,577$ tetrahedra. A close-up of both meshes can be seen in fig. 3.2. For both grids the structured inflation layer around the airfoil has a wall-normal thickness of 0.01. In the wall-normal direction the inflation layer
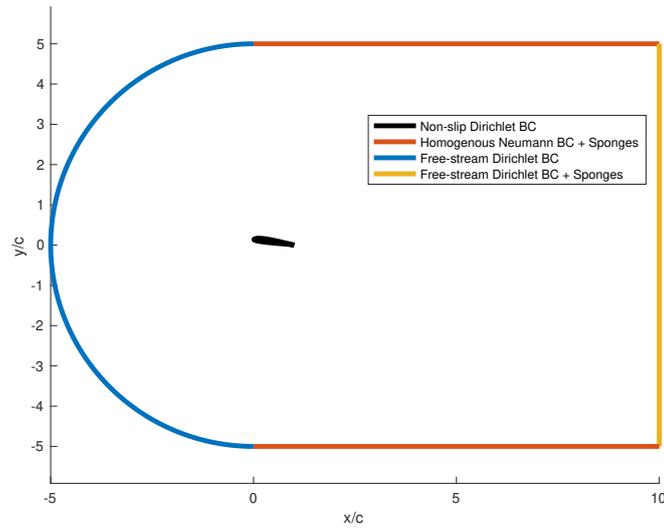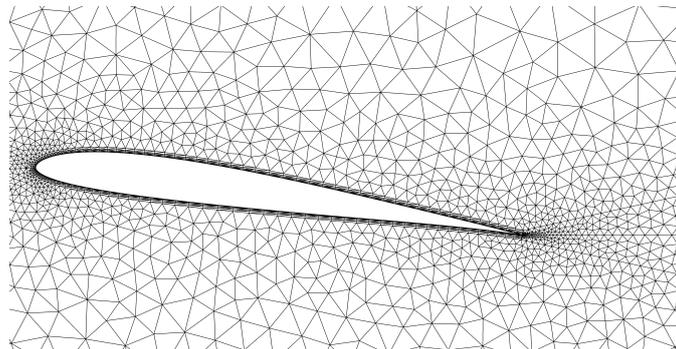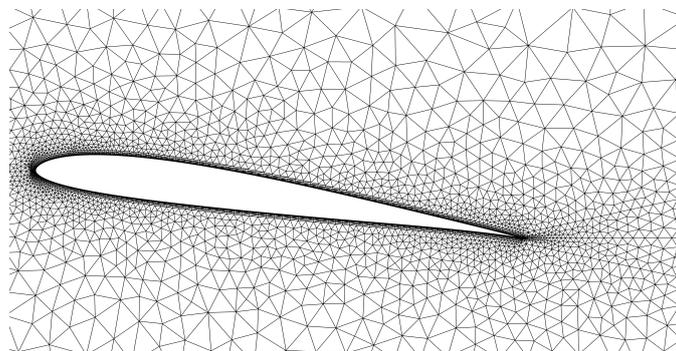
Figure 3.1: Computational domain and boundary conditions.

(a) Coarse mesh: 57 479 tetrahedron.

(b) Fine mesh: 110 577 tetrahedron.

Figure 3.2: 2D Close-up of the unstructured meshes adopted.

is divided into 4 hexahedra for the coarse mesh and 5 for the finer one. Each hexahedra is divided into $n_t = 6$ tetrahedra; hence, the resulting equivalent spacing of an hexahedral mesh is

$$\Delta_i = \frac{l_i}{\sqrt[3]{n_t}}, \tag{3.1}$$

where l_i is the length of the hexahedra in the i direction. To obtain an estimate of the distance between two points, the equivalent spacing Δ_i has to be further divided taking into account the polynomial degree of the approximated solution, i.e. the number of basis functions:

$$\delta_i = \frac{\Delta_i}{\sqrt[3]{n_\phi + 1}}, \tag{3.2}$$

where $n_\phi + 1 = \frac{1}{6}(q_K + 1)(q_K + 2)(q_K + 3)$ is the number of basis function and q_K is the order of the polynomial degree in the tetrahedron K. This value can be used to compute the first cell height in the in the wall-normal direction, i.e. $y_{1^{st},n} \equiv \delta_n|_{wall}$. It can be scaled with the viscous length to compute the $y^+_{1^{st},n}$[1] as done in section 3.1.5, changing the polynomial degree accordingly with the simulation.

The inflation layer around the airfoil and the near wake region up to $1.5c$ downstream the airfoil have been extruded in the z-direction with 6 layer for the coarse mesh and 8 for the finer one. The span-wise equivalent spacing δ_z/c will be reported for each simulation as well as the first cell height $y_{1^{st},n}$. In the remaining part of the domain the mesh is fully unstructured, also in the span-wise direction. The characteristic dimension of the cells at the inflow, outflow, upper and lower boundary $1c$.

Since the results obtained with fine mesh has been used also for the blade-vortex interaction simulation (see chapter 4), a refinement line upstream of the airfoil has been added to prevent the over dissipation of the vortex. The same line has been added also in coarse mesh so that also the results on this grid can be used, in future works, for the same purpose and, furthermore, it is also possible to make a meaningful comparison between the number of tetrahedra used in the two grids. Since this line does not affect the statistically steady flow, its details will be given in chapter 4.

The details of the grids are summarised in table 3.1. Note that the values reported here are independent from the polynomial degree of the simulation.

The xyz coordinates are the one linked to the domain (see again fig. 3.1), while ξ or `xi` will be used to indicate the coordinate parallel to the chord: $\xi = 0$ is the leading edge and $\xi = 1$ the trailing edge.

---

[1]The y^+ is the coordinate normal to the body surface and scaled with the viscous length scale $\delta_\nu \equiv \frac{\nu}{u_\tau}$, with $u_\tau \equiv \sqrt{\frac{\tau_w}{\rho}}$ and τ_w the wall shear stress. This new coordinate, i.e. $y^+ = y_n/\delta_\nu$, is of fundamental importance to study flows near the wall, for a number of reasons. The most important one is probably the fact that turbulent velocity profiles, scaled with the viscous velocity scale u_τ, at different Reynolds numbers, collapse on the same curve if plotted against the y^+ coordinate. See Pope, 2000 for the details.

Table 3.1: Details of the two meshes adopted.

Mesh	N. Elements	$\Delta_{1^{st},n}/c$ (N layers)	Δ_z/c (N layers)
Coarse	57 479	7.45×10^{-4} (4)	1.83×10^{-2} (6)
Fine	110 577	4.76×10^{-4} (5)	1.38×10^{-2} (8)

3.1.2 Boundary Conditions

The reference values L_r, ρ_r, u_r, T_r, introduced in section 2.1, are all unitary. On the surface of the airfoil non-slip, isothermal Dirichlet boundary condition is imposed, with $T_w = 1$. On the inflow and outflow boundary, Dirichlet conditions are enforced with the far field values $\mathbf{U}_\infty = (1, 0, 0)$ and $T_\infty = 1$. On the upper and lower boundary, homogenous Neumann conditions are imposed. Sponge layers have been applied on the outflow, on the upper and on the lower boundary to avoid reflections (see e.g. Crivellini, 2016 and Restelli and Giraldo, 2009 for sponges discussion). The boundary conditions are summarised in fig. 3.1.
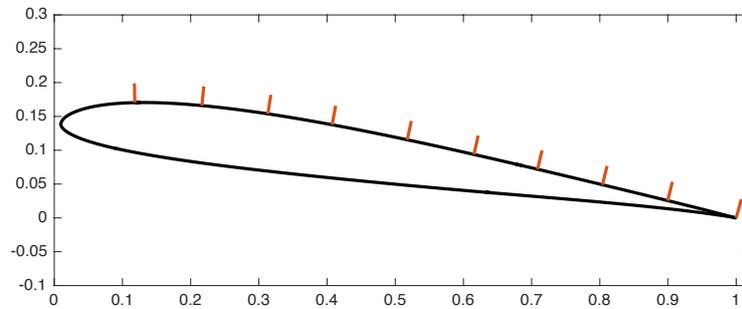
3.1.3 Points for the Acquisition of the Statistics

The points used to acquire the boundary layer velocity profiles are show in fig. 3.3. 20 points have been positioned every $0.1c$ from $0.1c$ to $1c$, perpendicularly to the local surface. The distance between two points increases parabolically with the wall distance to obtain a better resolution of the boundary layer velocity profiles (fig. 3.3b). For every chord-wise location, the last point is located at a distance from the surface of $0.0285c$. To average in the span-wise direction, 9 points (for each one of the 20 points in the perpendicular direction), with a constant spacing, have been used.

All the simulations have been run for sufficiently long time to obtain a fully developed flow before starting the statistics acquisition. The statistically statistically steady state condition has been verified.

3.1.4 Thresholds for *p*-adaptivity

Static $\mathbb{P}$-adaptive simulations have been performed using 2nd, 4th and 4th order polynomials. Some attempts have been done to introduce also the 5th order, but the simulations were unstable and, probably, a de-aliasing technique should be required. The thresholds used are $\epsilon_1 = 1.0 \times 10^{-4}$ to pass from the 2nd to the 3rd order and $\epsilon_2 = 1.0 \times 10^{-2}$ to pass from the 3rd to the 4th order. They have been chosen to match, approximately, the total number of degrees of freedom (DOF) of the uniform 3rd order simulation, as well as an acceptable distribution of polynomial degrees.

(a) Positions corresponding to chord-wise locations of $\xi = 0.1 - 1$ with 0.1 increments.
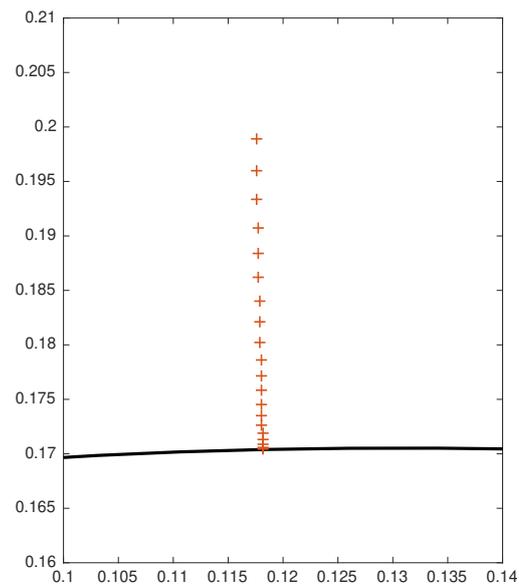
(b) Details of the 20 points used for the velocity profiles at the chord-wise location of 0.1.

Figure 3.3: Position of the points for the statistics acquisition. Note in (b) that the distance between two points becomes smaller near the wall for a better boundary layer resolution.

Table 3.2: Anisotropic model – Details of the simulations.

	Mesh	$y_{n,1\text{st}}/c$	δ_z/c	DOF	Δt
$\mathbb{P}^3$	Fine	1.75×10^{-4}	5.08×10^{-3}	$2\,211\,540$	1.2×10^{-5}
$\mathbb{P}^4$	Fine	1.45×10^{-4}	4.22×10^{-3}	$3\,870\,195$	1.1×10^{-5}
$\mathbb{P}$-adaptive	Fine	-	-	$1\,953\,460$	1.1×10^{-5}
$\mathbb{P}^4$	Coarse	2.27×10^{-4}	5.59×10^{-3}	$2\,011\,765$	1.7×10^{-5}

3.1.5 y^+ Estimate

The y^+ coordinate can be estimated from the friction coefficient C_f as follows:

$$
\begin{aligned}
y^+ = y_n/\delta_\nu = y_n u_\tau/\nu_r &= \frac{y_n}{\nu_r}\sqrt{\tau_w/\rho_r} = \frac{y_n}{\nu_r}\sqrt{C_f \frac{1}{2}\rho_r u_r^2 \frac{1}{\rho_r}} \\
&= \frac{y_n}{\nu_r}u_r\sqrt{C_f/2} = \frac{y_n}{c}\frac{\rho_r u_r c}{\mu_r}\sqrt{C_f/2} \\
&= \frac{y_n}{c}\,Re\,\sqrt{C_f/2}.
\end{aligned}
\tag{3.3}
$$

Hence, the first cell height scaled with the viscous length scale is

$$
y^+_{1\text{st}} = \frac{y_{n,1\text{st}}}{c}\,Re\,\sqrt{C_f/2}.
\tag{3.4}
$$

Since in LSB $C_f < 0$, the absolute value $|C_f|$ will be used in this region.

3.2 Resolution Dependence Analysis

Four simulations with the dynamic anisotropic model are compared for a grid convergence study and to validate the polynomial adaptivity technique: on the fine mesh uniform $\mathbb{P}^3$, $\mathbb{P}^4$ and $\mathbb{P}$-adaptive degree simulations are performed, while, on the coarse mesh, a uniform $\mathbb{P}^4$ degree simulation has been done. The time steps Δt used depend both on the (maximum) polynomial degree and on the mesh. They are reported in table 3.2 with the number of degrees of freedom (DOF) and the equivalent spacings introduced in section 3.1.1. The equivalent spacing for the $\mathbb{P}$-adaptive simulation cannot be defined because the polynomial degree can vary in all directions.

The *static p*-adaptive approach is performed: the value for the SF indicator required in the $\mathbb{P}$-adaptive simulation has been computed from a under-resolved $\mathbb{P}^2$ simulation and averaged over time (0.5 time units) before the adaption. After that the polynomial degree distribution remains unchanged. A 2D view of the resulting value of the indicator in the domain is shown in fig. 3.4 and the resulting polynomial degree distribution is shown in fig. 3.5. The indicator is able to capture the turbulent wake region as well as the boundary layer on the pressure side of the airfoil. A peak of the indicator can be observed near the stagnation point. From fig. 3.5a it can be observed that the 4$^{\text{th}}$ order is used also in the laminar

(a) Value of the SF indicator – Entire domain.

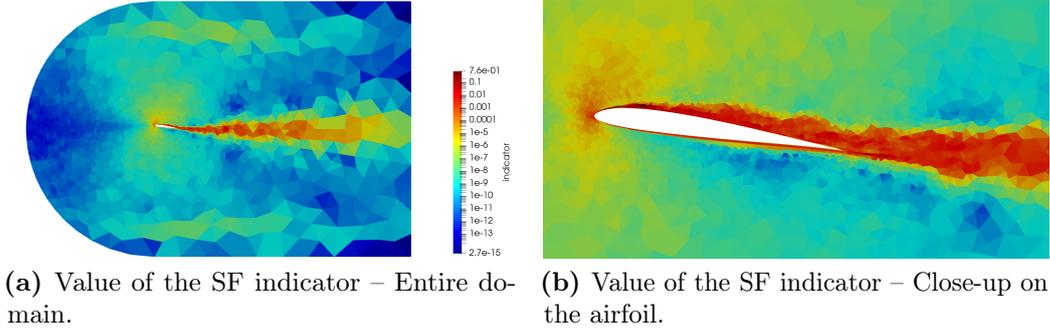**(b)** Value of the SF indicator – Close-up on the airfoil.

Figure 3.4: Value of the SF indicator (slice for $z = 0.2$) in logarithmic scale. It has been computed from a uniform under-resolved $\mathbb{P}^2$ simulation with the anisotropic model.
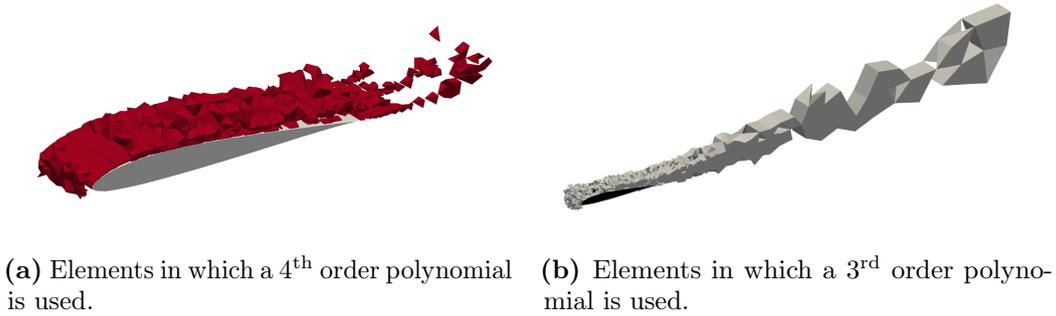

(a) Elements in which a 4th order polynomial is used.

(b) Elements in which a 3rd order polynomial is used.

Figure 3.5: Anisotropic model – Polynomial degree distribution obtained with the thresholds $\epsilon_1 = 1.0 \times 10^{-4}$ and $\epsilon_2 = 1.0 \times 10^{-2}$ applied to the SF indicator value of fig. 3.4.

shear layer and in the transitional region. Wang et al. (2019) performed $\mathbb{P}$-adaptive simulations (on the SD7003 test case) with a different feature-based indicator, finding polynomial distribution very similar to the one presented here.

Mean force coefficients are reported in table 3.3. They have been averaged for at least 2 convective time units and the statistical convergence has been verified. The moment coefficient has been computed with respect to the quarter of chord and positive clockwise, as usually done for airfoil analysis. Considering the 4th order solution on the fine mesh as reference, it can be observed that the force coefficients computed with the polynomial adaptivity are in good agreement, while the $\mathbb{P}^3$ and the $\mathbb{P}^4$ (on coarse mesh) order solutions are more scattered.

However, from fig. 3.6 which shows the mean (in time and in spanwise direction) pressure and friction coefficients, it can be observed that the solution obtained with the $\mathbb{P}^4$ on the coarse mesh is much closer to the reference than the $\mathbb{P}^3$ on the fine mesh, despite the higher number of DOF of the $\mathbb{P}^3$ simulation. This suggests that it is more advantageous to increase the order of the polynomial approximation rather than increase the resolution of the grid. The same conclusion can be found in the work of Bassi et al. (2016).

Concerning the mean separation and reattachment points reported in table 3.3, they have been extracted from the mean friction coefficient distribution of fig. 3.6b ($C_f = 0$ points). It is worth noting the very good agreement between the reattach-

Table 3.3: Anisotropic model –Force coefficients, separation and reattachment points for the different simulaitons.

	Force coefficients			LSB details	
	C_l	C_d	$C_{m,c/4}$	ξ_s	ξ_r
$\mathbb{P}^3$	0.9859	0.0410	-0.0192	0.026	0.211
$\mathbb{P}^4$	0.9738	0.0356	-0.0192	0.038	0.173
$\mathbb{P}$-adaptive	0.9693	0.0346	-0.0186	0.038	0.175
$\mathbb{P}^4$ Coarse mesh	0.9561	0.0354	-0.0176	0.046	0.179
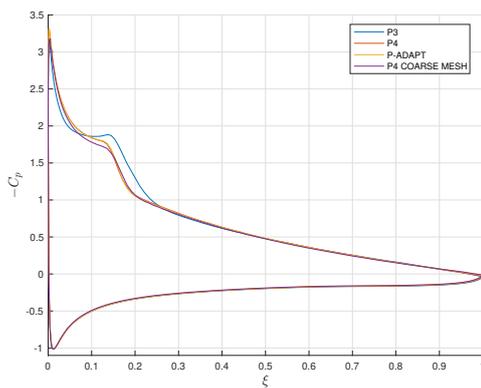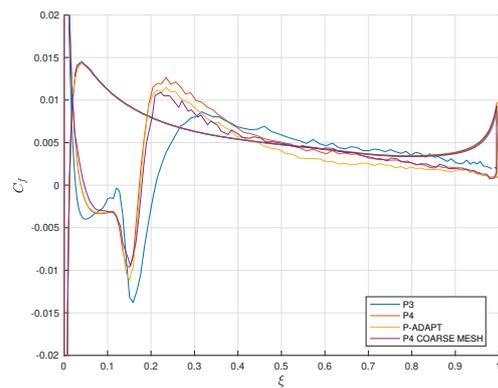
(a) Pressure coefficient.   **(b)** Friction coefficient.

Figure 3.6: Anisotropic model – Mean pressure and friction coefficients distributions.
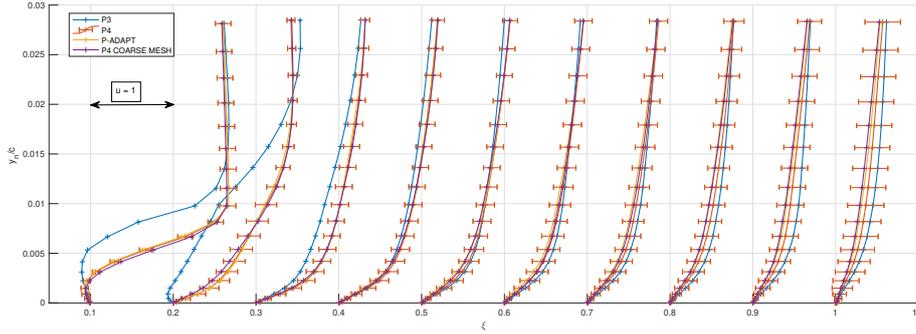
Figure 3.7: Anisotropic model – Profiles of mean x-component of velocity at chordwise locations $\xi = [0.1, \ldots, 1]$ on the suction-side.

ment points computed with the $\mathbb{P}^4$ simulations (both on the fine and on the coarse mesh) and the $\mathbb{P}$-adaptive one, while the $\mathbb{P}^3$ solution over-estimate the length of the LSB.

The mean velocity profiles of the x-component of the velocity at various chord locations are shown in fig. 3.7. Also in these plots the $\mathbb{P}^4$ solutions on the coarse and on the fine mesh and the $\mathbb{P}$-adaptive simulation are very close to each other. From the velocity profiles at $x/c = 0.1$ in fig. 3.7 it can be observed that the $\mathbb{P}^3$ solution over-estimates also the height of the LSB; this fact will be confirmed by instantaneous flow visualisations. After the reattachment points, all the simulations are in fair agreement.

The error bars in fig. 3.7 are reported only for the $\mathbb{P}^4$ degree simulation as an example. Following Nobach and Tropea, 2007, they have been computed as the statistical error estimate of a continuous signal: $\pm 2\sigma$ (95% of confidence) with

$$\sigma = u_{\mathrm{rms}}\sqrt{\frac{2T_x}{T}} \tag{3.5}$$

being u_{rms} the root-mean-square of the x-component of the velocity (see fig. 3.8), T_x the integral time scale of the velocity fluctuations and $T = 2.2$ the total observation time[2]. Quadrio and Luchini (2003) compute the integral time scale for $y^+ \to 0$ and for $y^+ = 10$ in a turbulent channel flow at $Re_\tau = 180$ finding, respectively, $T_x^+ = 19.1$ and $T_x^+ = 19.2$. The '+' superscript indicates that the time is scaled with the viscous time units which can be written as a function of the C_f: $t_\nu = \frac{2L_r}{Re\,u_r C_f}$. In a conservative way, $T_x^+ = 20$ has been chosen, while the values for the friction coefficient have been extracted from the distribution in fig. 3.6b. The error bars become significantly larger in the last chordwise locations since the C_f is lower.

In figs. 3.8 to 3.10 the (1,1), (2,2) and (1,2) components of the Reynolds stress tensor are shown at the same chord locations of the mean velocity profiles. It is worth noting the over-prediction of velocity fluctuations of the $\mathbb{P}^3$ simulation particularly in the first half of the chord, while the $\mathbb{P}^4$ and the $\mathbb{P}$-adaptive simulations are all in agreement.

---

[2]The simpler estimator $\sigma = u_{\mathrm{rms}}/\sqrt{N}$, with N the number of samples, can not be used since the samples are strongly correlated.
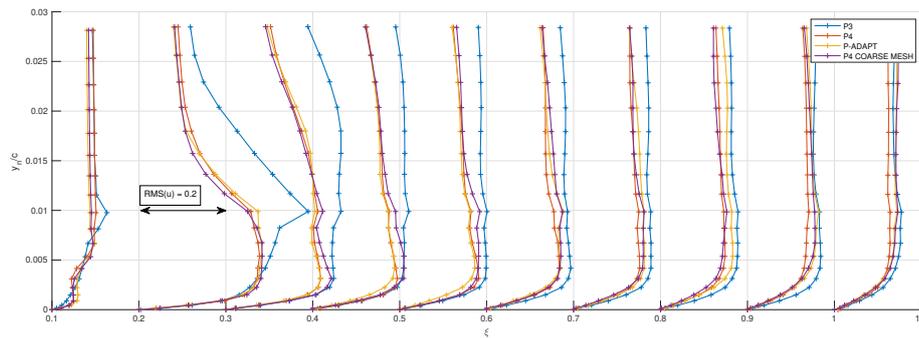
Figure 3.8: Anisotropic model – RMS of x-component of velocity, i.e. $\sqrt{\langle u'^2 \rangle}/u_r$, at chordwise locations $\xi = [0.1, \ldots, 1]$ on the suction-side.
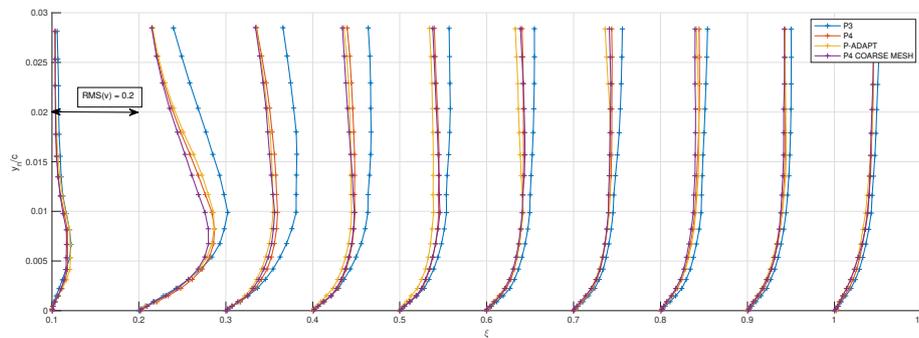
Figure 3.9: Anisotropic model – RMS of y-component of velocity, i.e. $\sqrt{\langle v'^2 \rangle}/u_r$, at chordwise locations $\xi = [0.1, \ldots, 1]$ on the suction-side.
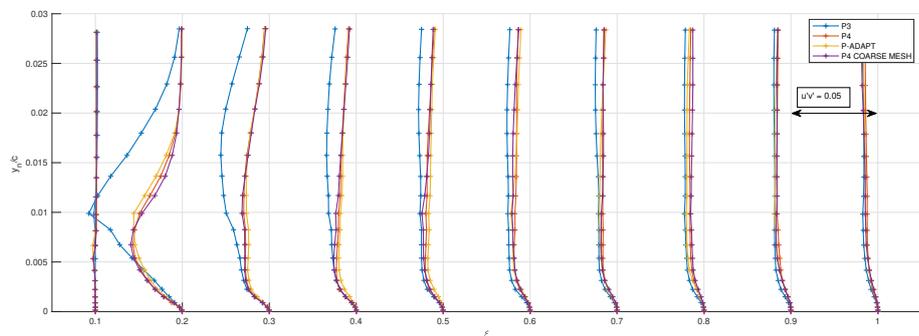
Figure 3.10: Anisotropic model – Profiles of mean xy-component of Reynolds stresses tensor, i.e. $\langle u'v' \rangle /u_r^2$, at chordwise locations $\xi = [0.1, \ldots, 1]$ on the suction-side.
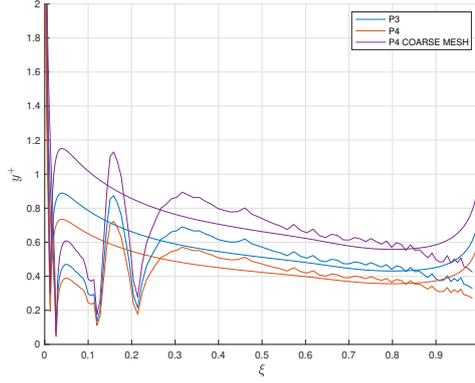
Figure 3.11: First point height in wall unit obtained applying the eq. (3.4). The friction coefficient distribution of the $\mathbb{P}^4$ solution (fig. 3.6b) has been used.

An estimate of the first point height in y^+−coordinate is show in fig. 3.11 for only the uniform degree simulations. It has been computed applying eq. (3.4) and using the friction coefficient distribution of the $\mathbb{P}^4$ simulation. Concerning the $\mathbb{P}$-adaptive simulation, since the polynomial degree can change also in the third dimension, an estimate of the y^+−coordinate can not be computed rigorously. However, since the polynomial degree in the boundary layer is 3 or 4, it can be stated that the curve is always between the red ($\mathbb{P}^4$) and blue one ($\mathbb{P}^3$). The first point height is below $y^+ = 1$ for all the simulations on the fine mesh with the exception of a small part near the stagnation point where the friction coefficient tends to infinity. On the coarse mesh, the first point height is slightly above 1 after the reattachment point and on the first part of the pressure-side, but, as shown in the previous results, it does not seem to affect the accuracy.

In fig. 3.12 a comparison between the dimensions of the instantaneous separated flow region can be done. In particular, it can be observed the confirmation of what it has been observed in the mean velocity profiles: the height of the recirculating region is greater in the uniform $\mathbb{P}^3$ simulation (fig. 3.12a) than in all the others. Moreover, in fig. 3.12b particularly, the Kelvin–Helmholtz (KH) instability, which triggers the transition to turbulence in the free shear layer, can be easily seen. There are no evident differences between the flow fields of the $\mathbb{P}^4$ and the $\mathbb{P}$-adaptive simulations (figs. 3.12b to 3.12d).

The over-estimation of both the height and the length of the recirculating region of the $\mathbb{P}^3$ simulation has been explained with an excessive dissipation which suppresses the KH instability. Consequently, the transition to turbulence is delayed and the reattachment of the BL moves downstream.

In conclusion, it can be stated that:

- the $\mathbb{P}^3$ solution is under-resolved and too dissipative to correctly represent the flow;

- the results of the $\mathbb{P}^4$ degree simulation on the coarse grid are close enough to the reference to state that the resolution of the $\mathbb{P}^4$ simulation on the fine grid is sufficient;
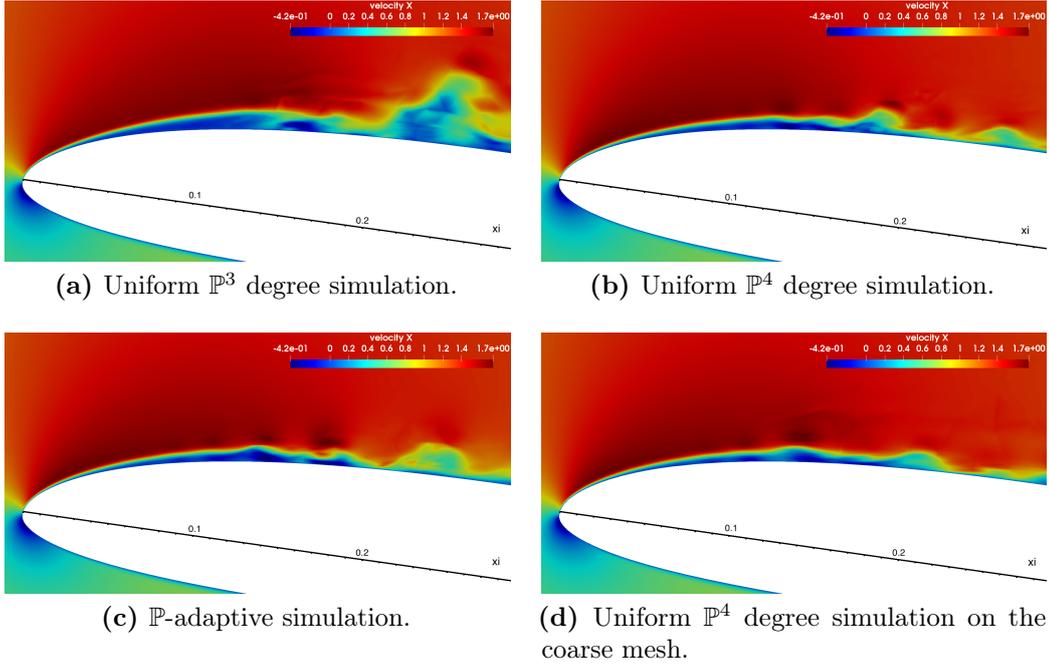
(a) Uniform $\mathbb{P}^3$ degree simulation.

(b) Uniform $\mathbb{P}^4$ degree simulation.

(c) $\mathbb{P}$-adaptive simulation.

(d) Uniform $\mathbb{P}^4$ degree simulation on the coarse mesh.

Figure 3.12: Anisotropic model – Slice for $z = 0.2$ of the instantaneous x-component of the velocity field showing a comparison between the different simulations of the dimension of the separated flow region.

- the $\mathbb{P}$-adaptive simulation results are very close to the reference and, hence, the polynomial adaptivity technique is able to correctly represent the flow with a great saving in the computational cost (50% of the $\mathbb{P}^4$ DOF, see again table 3.3).

Because of that, in section 3.4 only the results obtained with $\mathbb{P}^4$ degree on the fine mesh and the $\mathbb{P}$-adaptive simulation will be used as comparison with literature and with the results coming from the ILES (see section 3.3).

3.3   Implicit LES Results

The implicit modelling have been extensively used in literature to simulate the flow around the SD7003 (see e.g. Bassi et al., 2016, Boom and Zingg, 2013 and Uranga et al., 2009), hence two ILES are here presented and will be compared in section 3.4 with the LES results obtained with the anisotropic model. Differently from what usually done in literature, it has not been added any additional numerical dissipation, artificial diffusion or regularisation of the computed solution: the subgrid scale contributions to the Navier–Stokes equations are simply dropped, leading, basically, to an under-resolved DNS. Thanks the very good results of the $\mathbb{P}$-adaptive simulation with the anisotropic model, only a uniform $\mathbb{P}^3$ degree and a $\mathbb{P}$-adaptive simulation have been done. In this case, the SF indicator for the polynomial adaptivity has been computed from the $\mathbb{P}^3$ ILES simulation. The resulting polynomial distribution is shown in fig. 3.13. It can be observed that the distribution is quite different from the one presented in the previous section

(a) Elements in which a 4th order polynomial is used.

(b) Elements in which a 3rd order polynomial is used.

Figure 3.13: Implicit model – Polynomial degree distribution obtained with the thresholds $\epsilon_1 = 1.0 \times 10^{-4}$ and $\epsilon_2 = 1.0 \times 10^{-2}$.

Table 3.4: Implicit model – Details of the simulations.

	Mesh	$y_{n,1^{\text{st}}}/c$	δ_z/c	DOF	Δt
$\mathbb{P}^3$ ILES	Fine	1.75×10^{-4}	5.08×10^{-3}	$2\,211\,540$	1.1×10^{-5}
$\mathbb{P}$-adaptive ILES	Fine	-	-	$1\,968\,220$	1.1×10^{-5}

(fig. 3.5). The time steps used, the number of DOF and the equivalent spacings are reported in table 3.4. The total number of DOF and the equivalent spacings of the $\mathbb{P}^3$ ILES is, of course, the same of the $\mathbb{P}^3$ with the anisotropic model, while the time step has been reduced for stability reasons.

The time step reported for the $\mathbb{P}$-adaptive ILES has been used to reach the steady state condition and to acquire the statistics for only 1 convective time unit (instead of the 2 or 3 of all the other simulations). After that, the simulation becomes unstable and it was not possible to acquire more statistics also with a reduction of the time step. Because of that, the not fully converged statistics of the $\mathbb{P}$-adaptive ILES will be marked with ' * ' in the following tables and with dashed curves in the figures: the comparisons with this simulation must be interpreted as *tendencies*. However the pressure and friction coefficient distributions have not changed in the last 0.5 convective time unit, and, hence, they can be supposed to be close to an hypothetical fully converged solution. It is highlighted once more that no artificial dissipation has been added in the present ILES simulations, differently of what usually done in literature for stability purposes.

The mean force coefficients, separation and reattachment points (computed as the first and last $C_f = 0$ points) are reported in table 3.5. While the force coefficients and the separation points are in a good agreement, the flow reattaches downstream in the $\mathbb{P}^3$ ILES leading to a larger recirculating region, similarly to what already seen in the results of the anisotropic model. Furthermore a secondary and smaller reverse-flow region is present in both the ILES as it can be clearly seen from the $C_f < 0$ regions in fig. 3.14b. Between the two revers-flow regions where, the flow is going in the $-x$-direction, there is a small region where $C_f > 0$, hence the flow is going in the $+x$-direction. This could be explained as a tiny recirculating region where the flow, averaged in time and in the spanwise direction, is rotating

Table 3.5: Implicit model –Force coefficients, separation and reattachment points for the different simulations. * indicates the not fully converged statistics.

	Force coefficients			LSB details	
	C_l	C_d	$C_{m,c/4}$	ξ_s	ξ_r
$\mathbb{P}^3$ ILES	0.9758	0.0518	-0.0153	0.021	0.335
$\mathbb{P}$-adaptive ILES	0.9817*	0.0489*	-0.0164*	0.023*	0.281*

(a) Pressure coefficient.

(b) Friction coefficient.
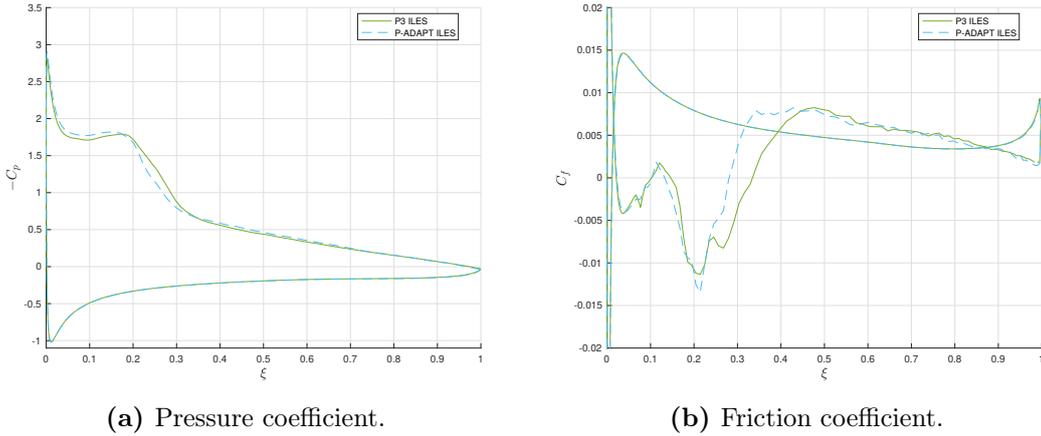
Figure 3.14: Implicit model – Mean pressure and friction coefficients distributions.

counter-clockwise.

The mean x-component of the velocity profiles is plotted in fig. 3.15. As expected from the previous discussion, the major differences between the two ILESs are in the first three chord locations. The error bars shown here for the $\mathbb{P}$-adaptive ILES have been computed as previously done in section 3.2, i.e. $\pm 2\sigma$; they are larger not only because of the larger values of u_{rms} (see fig. 3.16), but, mostly, as a result of the unstable simulation which allows a shorter observation time (only 1 convective time unit). Recall that $\sigma = u_{\text{rms}}\sqrt{\frac{2T_x}{T}}$ and T_x is the integral time scale computed, in this case, with the C_f distribution from the $\mathbb{P}$-adaptive ILES.

In figs. 3.16 to 3.18 the RMS of x and y-component of the velocity and the xy-component $\langle u'v' \rangle$ of the Reynolds stress tensor are plotted. While in section 3.2 the overshoot in the Reynolds stresses was clear for the more dissipative simulation (uniform $\mathbb{P}^3$), in this case there is not a recognisable overshoot of one solution over the other. This suggests possible a lack of resolution also of the $\mathbb{P}$-adaptive ILES. However, increasing the spatial resolution of an ILES, not only would require a higher computational cost, but, most importantly, would also require an artificial dissipation to be added to suppress the instabilities coming from the high order discretisation. The right amount of artificial dissipation to be added is still a subject of ongoing research (see e.g. Boom and Zingg (2013)): it must be tuned in order to stabilise the simulation without compromise the accuracy of the solution. Since this topic goes beyond the scope of the present work, others ILESs have not been done.
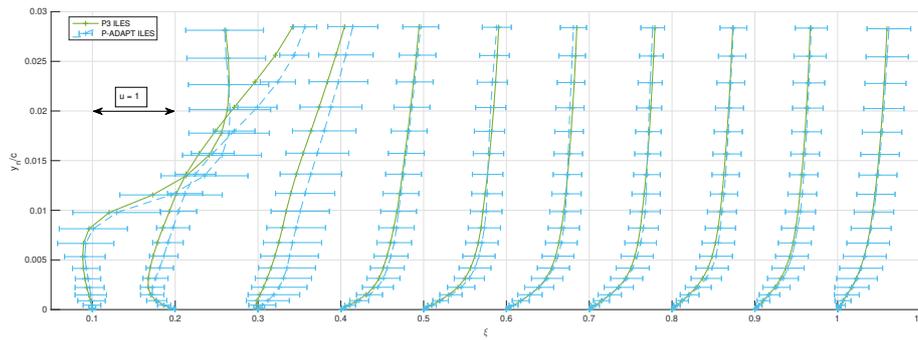
Figure 3.15: Implicit model – Profiles of mean x-component of velocity at chordwise locations $\xi = [0.1, \ldots, 1]$ on the suction-side.
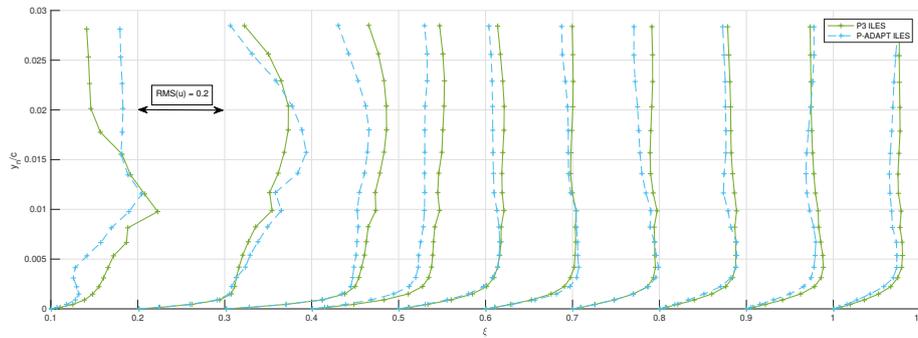

Figure 3.16: Implicit model – RMS of x-component of velocity, i.e. $\sqrt{\langle u'^2 \rangle}/u_r$, at chordwise locations $\xi = [0.1, \ldots, 1]$ on the suction-side.
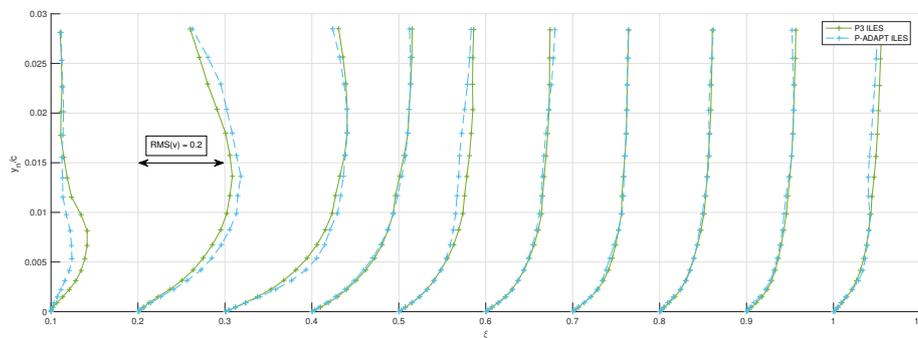

Figure 3.17: Implicit model – RMS of y-component of velocity, i.e. $\sqrt{\langle v'^2 \rangle}/u_r$, at chordwise locations $\xi = [0.1, \ldots, 1]$ on the suction-side.
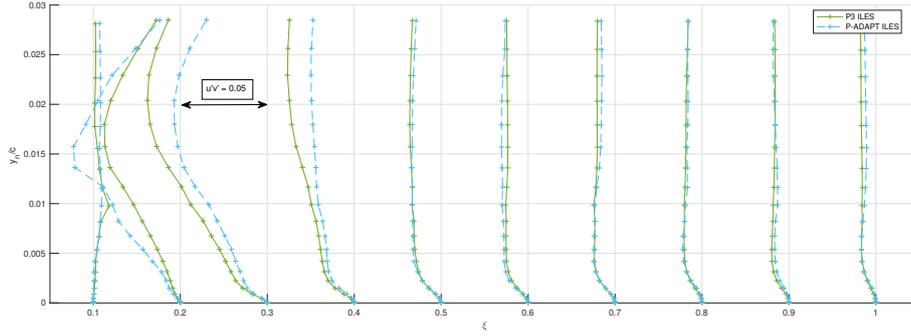
Figure 3.18: Implicit model – Profiles of mean xy-component of Reynolds stresses tensor, i.e. $\langle u'v' \rangle /u_r^2$, at chordwise locations $\xi = [0.1, \ldots, 1]$ on the suction-side.

Flow visualisations will be shown in section 3.4 for comparison with the anisotropic model results and they confirm the larger recirculating region of the $\mathbb{P}^3$ ILES with respect to the $\mathbb{P}$-adaptive ILES.

In conclusion, it can be stated that:

- the uniform $\mathbb{P}^3$ ILES lacks of spacial resolution since the results differ from the $\mathbb{P}$-adaptive ILES, in particular in the estimation of the dimension of the LSB;

- the $\mathbb{P}$-adaptive ILES is unstable and the results obtained are not fully converged; furthermore, from the comparison of the Reynolds stresses profiles, there is not a clear overshoot of the $\mathbb{P}^3$ simulation over the $\mathbb{P}$-adaptive , as observed in the LES with the anisotropic closure. This could suggest a lack of spacial resolution also of the $\mathbb{P}$-adaptive ILES. Indeed it is actually an under-resolved DNS, so a model for the subgrid scale contribution is important also for stability reasons.

However, as observed in the anisotropic model results (see section 3.2), the polynomial adaptivity is able to provide a better accuracy than the $\mathbb{P}^3$ simulation. Because of that, in section 3.4, the $\mathbb{P}$-adaptive ILES results will be used to give a qualitative tendency of an implicit model computation, while the $\mathbb{P}^3$ ILES results will not be shown.

3.4 Comparison and Discussion

The results presented in the previous sections ($\mathbb{P}$-adaptive LES, $\mathbb{P}$-adaptive ILES and the $\mathbb{P}^4$ degree LES) are here compared with experimental measurements and other numerical simulations available in literature. Since the RANS models are tuned using the more accurate (I)LES results (see e.g. Catalano and Tognaccini, 2011), only (I)LES are considered for comparison. Unfortunately the only DNS available for this test case has been made by Ducoin, Loiseau, and Robinet, 2015 for $\alpha = 4°$.

Another powerful tool available is XFOIL which has been proven to be very accurate in the prediction of separation and reattachment points at low Reynolds

numbers (see Drela, 1989). XFOIL uses the solution from an inviscid panel method as the starting point for an iterative viscous formulation which employs integral momentum and kinetic energy shape parameter equations. The transition point is located through the e^N-method which models the growth of perturbations: the transition occurs when N reaches a user-specified critical value N_{cr}. This value is usually related to the background disturbance (turbulence) level T_u of the experimental facility. Two values have been used: $N_{\text{cr}} = 6$ ($T_u = 0.245$) has been chosen to match approximately the experimental $T_u \approx 0.28\%$ of Hain et al. (2009); $N_{\text{cr}} = 9$ ($T_u = 0.07\%$) has been considered as representative for the (nominally) zero background turbulence level in a LES. Higher values of N_{cr} cause severe difficulties in the convergence of XFOIL iterative method and the predictions are no longer reliable. XFOIL takes also into account the compressibility effects through the Karman–Tsien correction applied to the pressure coefficient and to the so called *dynamic pressure*, i.e. $q = \frac{1}{2}\rho_\infty U_\infty^2$. Both incompressible and compressible results with $Ma = 0.2$ will be considered. The angle of attack of the XFOIL simulation was set to $\alpha = 8°$.

3.4.1 Mean Flow Features

In table 3.6 the force coefficients and the details of the LSB are reported for a number of experimental and numerical studies, as well as for the present work. Force coefficients are quite scattered (also if only $Ma = 0.1$ results are considered) and, most of them, overshoot the experimental measurements of Selig (1995) (name in table: UIUC Wind T.), probably because of the higher Mach number. However the force coefficients of the $\mathbb{P}^4$ and $\mathbb{P}$-adaptive LESs of the present work agree very well with the work of Boom and Zingg (2013) ($\mathcal{O}(4)$ SBP ILES) and Garmann et al. (2013)($\mathcal{O}(6)$ FD ILES). The drag coefficient of the $\mathbb{P}$-adaptive ILES is more aligned with the ILES results of Bassi et al. (2016) ($\mathbb{P}^4$ DG ILES and $\mathbb{P}^3$ DG ILES) and Wang et al. (2019) ($\mathbb{P}$-adapt. FR ILES), while the (qualitative) overshoot of the $\mathbb{P}$-adaptive ILES lift coefficient on all the other results (except for XFOIL) can be only partially explained with the higher Mach number and, probably, it is most due to the not fully converged value.

The major differences between all the studies are in the prediction of the LSB characteristic points: separation, transition and reattachment. Experimental measurements are strongly affected by the turbulence level T_u of the facility (see e.g. Herbst et al., 2018): while the separation point moves downstream with an increase of T_u, the transition and the reattachment points move upstream. The overall effect is a reduction in the total LSB dimension until, for very high turbulence levels, the LSB disappears completely. The AFRL dataset of Ol et al. (2005) (AFRL Water T.) place separation at 0.05 and reattachment at 0.16; however, it has to be remarked that the recirculating region in this experiment is not visible by means of streamlines because of a lack in the PIV spacial resolution and, furthermore, it is not clear how the points have been computed. Because of that they have been marked with a '*' in table 3.6. Instead, the trend described by Herbst et al. (2018) is identifiable for transition and reattachment points in the experiments of Hain et al. (2009) (WUB Water T.1) and Burgmann and Schröder (2008) (Water T.), with $T_u \approx 0.28\%$ and $T_u = 1\%$ respectively. On the other hand the separation point

seems to have the opposite trend.

With $N_{cr} = 6$ ($T_u = 0.245\%$), separation, transition and reattachment points computed by XFOIL are all collocated upstream with respect to the experimental measurements of Hain et al. (2009) (WUB Water T.1). However it is worth noting that the trend for the separation point for an increase of the T_u confirms the experimental one. For $N_{cr} = 9$ ($T_u = 0.07\%$) an increase in the Mach number leads to an upstream movement of the computed LSB.

Regarding the numerical computed LSBs available in literature, they place the separation at $\xi_s \approx 0.03$ and the reattachment at $\xi_r \approx 0.29$, which are in a very good agreement with the $\mathbb{P}$-adaptive ILES presented here, but rather far from the experimental measurements and XFOIL predictions. Instead, the $\mathbb{P}$-adaptive and the $\mathbb{P}^4$ LESs with the dynamic anisotropic model predict a location for separation and reattachment which is midway between experimental results and XFOIL predictions: the separation is delayed and the transition and reattachment appear upstream with respect to the (I)LESs available in literature. This behaviour could be assimilated with a simulation with a small amount of turbulence background level, as suggested by experiments and numerical simulations (see Breuer, 2018). However the source of these disturbs it is not something artificially introduced by numerical errors, but it is related to the turbulence modelling. Indeed:

- if in the $\mathbb{P}$-adaptive simulation the disturbs would come from the polynomial adaptivity, they should not be present in the uniform $\mathbb{P}^4$ simulation (but the results of these two simulations are almost identical);

- all the remaining possible disturbs coming from the DG discretisation (i.e. not related to the turbulence model) should also be present in the $\mathbb{P}$-adaptive ILES, but this is not the case, since the separation and reattachment points are in completely different locations and in a good agreement with the other numerical results.

Therefore the source of the disturbs is, for sure, related to the turbulence modelling. To better comprehend why and if the anisotropic model could provide better results compared to the implicit model it is necessary to analyse which are the physically important phenomena involved in this type of flow.

In the recent work of Cimarelli, Leonforte, De Angelis, Crivellini, and Angeli (2019) a DNS of the flow around a rectangular cylinder of dimensions $(L_x, L_y) =$

---

[3] Selig, 1995

[4] Ol et al., 2005

[5] Hain et al., 2009, $Re = 66\,000$

[6] Radespiel et al., 2007

[7] Burgmann and Schröder, 2008

[8] Qin et al., 2018

[9] Catalano and Tognaccini, 2009

[10] Bassi et al., 2016

[11] Bassi et al., 2016

[12] Wang et al., 2019

[13] Galbraith and Visbal, 2008

[14] Garmann et al., 2013

[15] Boom and Zingg, 2013

Table 3.6: Comparison between literature and present work results on the SD7003 airfoil at $Re = 60\,000$ and $\alpha = 8°$. Acronyms: Finite Differences (FD); Discontinuous Galerkin (DG); Flux Reconstruction (FR); Compact Finite Differences (CFD); Summation-By-Parts (SBP). Experimental acronyms refer to the specific facility or institution. * indicate not fully converged statistics or unclear experimental results.

|		Mach	Force coefficients			LSB details		
			C_l	C_d	$C_{m,c/4}$	ξ_s	ξ_t	ξ_r
Experimental results								
UIUC Wind T.[3]	$T_u < 0.1\%$	< 0.01	0.936	0.0299	-	-	-	-
AFRL Water T.[4]	$T_u < 0.1\%$	-	-	-	-	0.05*	-	0.16*
WUB Water T.1[5]	$T_u \approx 0.28\%$	-	-	-	-	0.078	0.147	0.205
WUB Water T.2[6]	$T_u = 0.8\%$	-	-	-	-	-	0.136	-
Water T.[7]	$T_u = 1\%$	< 0.01	-	-	-	0.05	0.125	0.135
Numerical results								
$\mathcal{O}(2)$ LES FD[8]		Inc.	0.93	0.040	-	0.042	0.16	0.25
$\mathcal{O}(2)$ LES FD[9]		Inc.	≈ 0.95	≈ 0.044	-	≈ 0.03	-	≈ 0.28
$\mathbb{P}^3$ DG ILES[10]		0.1	0.9441	0.0457	-0.0223	0.028	-	0.303
$\mathbb{P}^4$ DG ILES[11]		0.1	0.9534	0.0454	-0.0224	0.027	-	0.294
$\mathbb{P}$-adapt. FR ILES[12]		0.1	0.9270	0.0470	-	0.0301	-	0.3123
$\mathcal{O}(6)$ CFD ILES[13]		0.1	-	-	-	0.04	0.18	0.28
$\mathcal{O}(6)$ FD ILES[14]		-	0.9696	0.0391	-0.0197	0.023	-	0.259
$\mathcal{O}(4)$ SBP ILES[15]		0.2	0.968	0.034	-	0.037	0.105	0.20
Present work								
XFOIL $N_{cr} = 6$	$T_u = 0.245\%$	Inc.	0.978	0.0305	-0.0179	0.018	0.130	0.148
XFOIL $N_{cr} = 9$	$T_u = 0.07\%$	Inc.	0.991	0.0360	-0.0175	0.019	0.160	0.195
XFOIL $N_{cr} = 9$	$T_u = 0.07\%$	0.2	1.003	0.0394	-0.0153	0.017	0.152	0.190
$\mathbb{P}^4$ LES DG		0.2	0.9738	0.0356	-0.0192	0.038	$\lesssim 0.1$	0.173
$\mathbb{P}$-adapt. LES DG		0.2	0.9693	0.0346	-0.0186	0.038	$\lesssim 0.1$	0.175
$\mathbb{P}$-adapt. ILES DG		0.2	0.9817*	0.0489*	-0.0164*	0.023*	< 0.2	0.281*

$(5D, D)$ has been proposed. This is a common test case studied experimentally and numerically. The main flow feature is the same of the present work, i.e. a laminar separation and a transition to turbulence in the free shear layer triggered by a KH instability and followed by a turbulent reattachment. An *a priori* analysis[16] has been performed finding an intense energy backscatter (see section 2.2) from the subgrid field to both the mean and fluctuating flow fields. This phenomenon is located in all the shear layer and, hence, it has severe influences on the transition and, consequently, on the reattachment point (see e.g. Saathoff and Melbourne, 1997, Alam and Sandham, 2000 and Abdalla and Yang, 2004). The backscatter phenomenon has been found also in the near-wall reverse BL. In the aforementioned article of Cimarelli et al. (2019), it is also remarked that the phenomenon of reverse energy transfer should be taken into account by subgrid closures because the wrong prediction of the subgrid stresses in the shear layer could have a significant impact on the mean reattachment point. The very same conclusions can be found in the work of Piomelli, Cabot, Moin, and Lee (1991) and Piomelli, Zang, Speziale, and Hussaini (1990) where "It was found that the standard residual stress models are excessively dissipative; they erroneously delay the onset of transition in the large-eddy simulation of boundary layers, leading to considerable error."

Since the implicit model is intrinsically not able to capture the reverse energy cascade, it is probably not suitable to model the transitional flow around the SD7003 airfoil. The effect is exactly the one described by Piomelli et al. (1990): the lack of the energy, which should come from the backscatter, delays the KH instability and, as a result, the reattachment point. On the other hand, the dynamic anisotropic model used in the $\mathbb{P}$-adaptive and $\mathbb{P}^4$ simulations is able to capture this phenomenon. However it is possible that it overshoots the amount of the energy coming from the subgrid scales, leading to a too early transition and reattachment, but, since a DNS dataset is not available, this hypothesis is based only on the comparison with experimental measurements at lower Mach number.

The influence of the subgrid model on the SD7003 test case at $Re = 60\,000$ and $\alpha = 4°, 8°$ (the Mach number has not been reported) has been studied by Garmann et al. (2013) (table name: $\mathcal{O}(6)$ FD ILES). They proposed a comparative study between the results obtained with ILES and LES with Smagorinsky dynamic closure (see section 2.2.2), finding very similar results. In table 3.6 only the ILES results are reported, because only the last digit changes in the LES. Recall that the Smagorinsky dynamic model is, in principle, able to capture the reverse energy cascade. However, in the implementation proposed by Garmann et al. (2013), a spanwise averaging of the dynamically-computed Smagorinsky constant has been done to stabilise the simulation, resulting in a possible reduction of the backscatter.

The only ILES available in literature (as far as the author knowledge) which obtains results very similar with the LESs of the present work, is the one proposed by Boom and Zingg (2013) ($\mathcal{O}(4)$ SBP ILES). The separation and reattachment points has been found, respectively, in 0.037 and 0.20, and also lift and drag coefficients are in a very good agreement with the ones computed in the present work. This fact

---

[16]The *a priori* analysis is a common practice to asses the LES approach in a particular test case. It consists in filtering the DNS flow field and in comparing the behaviour of the resolved field and the subgrid stresses with the unfiltered DNS dataset.
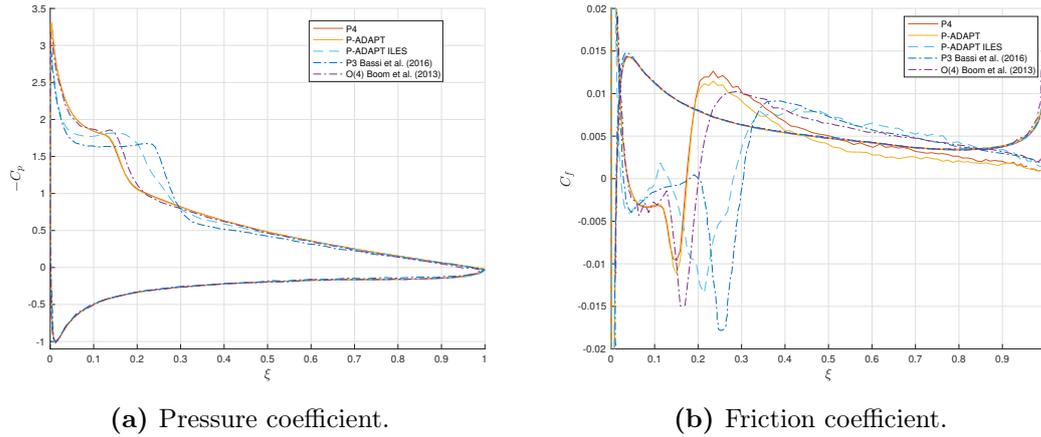
(a) Pressure coefficient.

(b) Friction coefficient.

Figure 3.19: Comparison between pressure and friction coefficient distributions of the $\mathbb{P}^4$, $\mathbb{P}$-adaptive LES and $\mathbb{P}$-adaptive ILES of the present work with the results of Bassi et al. (2016) and Boom and Zingg (2013).

presently lacks of a good explanation, but two possible reasons are here proposed:

- the extremely fine mesh adopted (4.9×10^6 DOF) reduces the amount of numerical diffusion coming from the discretisation;

- the numerical diffusion added to stabilise the simulation has been carefully tuned to match the DNS results in a different test case (Taylor–Green vortex).

As a result the total amount of dissipation added is probably very small compared to the other ILESs. Hence, the disturbances are not suppressed and the KH instability is triggered earlier, leading to a smaller (less diffused) LSB.

Friction and pressure coefficients of the present work are compared in fig. 3.19 with the results of the aforementioned article of Boom and Zingg (2013) ($\mathcal{O}(4)$ SBP ILES) and with the results of Bassi et al. (2016) ($\mathbb{P}^3$ DG ILES). The last ones are representative for the majority of ILESs. Major differences between the LESs of the present work and the ILES of Bassi et al. (2016) can be seen not only in the C_f but also in the C_p distribution. The lower peak in the C_p on the suction side of the ILES of Bassi et al. (2016) is also present in the $\mathbb{P}$-adaptive LES of the present work and it is probably due to the over-diffusion. It is worth noting that the $\mathbb{P}$-adaptive ILES is midway between the LES of the present work and the majority of ILESs, suggesting that a more resolved, stabilised (and fully converged) $\mathbb{P}$-adaptive ILES would probably be even closer to the results of Bassi et al. (2016). The pressure coefficient distribution of the LES with the anisotropic closure and the ILES of Boom and Zingg (2013) are in a very good agreement.

The mean velocity profiles are shown in fig. 3.20 and confirm the great differences between the LESs with the anisotropic model and the $\mathbb{P}$-adaptive ILES. The LSB is not only longer in the ILES, but also much thicker at $\xi = 0.1$. In the second half of the airfoil the higher velocity in the ILES boundary layer confirms the higher friction coefficient observed in fig. 3.19b.

For completeness, the RMS of x and y-component of the velocity and the
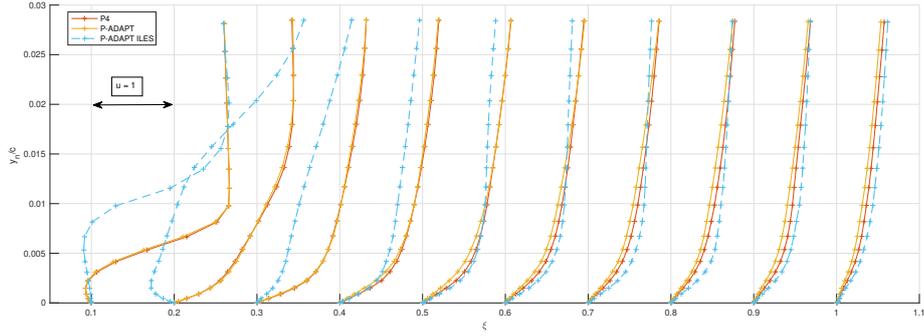
Figure 3.20: Comparison between $\mathbb{P}^4$ and $\mathbb{P}$-adaptive LESs and $\mathbb{P}$-adaptive ILES – Profiles of mean x-component of velocity at chordwise locations $\xi = [0.1, \ldots, 1]$ on the suction-side.
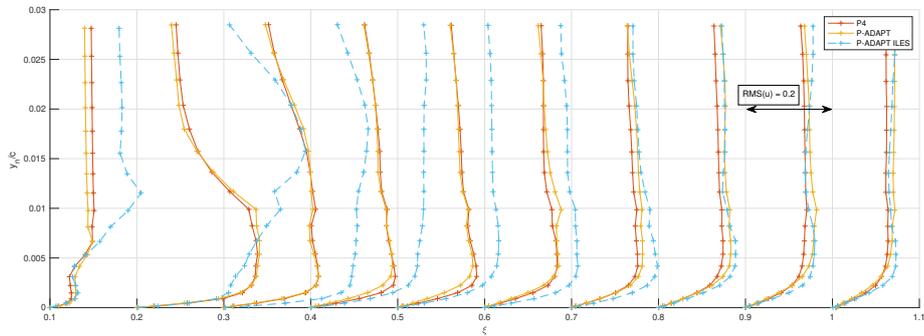

Figure 3.21: Comparison between $\mathbb{P}^4$ and $\mathbb{P}$-adaptive LESs and $\mathbb{P}$-adaptive ILES – RMS of x-component of velocity, i.e. $\sqrt{\langle u'^2 \rangle}/u_r$, at chordwise locations $\xi = [0.1, \ldots, 1]$ on the suction-side.

xy-component of the Reynolds stresses are shown in figs. 3.21 to 3.23, once more highlighting the differences between the LESs and the ILES.

The criterion for the choice of the transition points reported in table 3.6 is not uniform between the different authors and, hence, they must be interpreted carefully. For example Ol et al. (2005) and Hain et al. (2009) place the transition onset at stream-wise location where the normalised Reynolds stress $-\langle u'v' \rangle /u_r^2$ first reaches a arbitrary value of 0.001. XFOIL place the transition point where N reaches the user-specified value N_{cr} (i.e. the e^N method for the prediction of disturbances). Another approach, proposed by McAuliffe and Yaras (2005), place the transition onset at the stream-wise coordinate in which the growth rate of $-\langle u'v' \rangle$ deviates from the exponential path[17]. Since in the present work the flow statistics far from the wall are available at discrete chord-wise locations, the transition point cannot be determined precisely with this last criterion. However for the $\mathbb{P}^4$ and the $\mathbb{P}$-adaptive LESs at $(\xi, y_n/c) = (0.1, 0.0053)$ the (1,2) component of the Reynolds stresses are, respectively, $-\langle u'v' \rangle /u_r = 0.00126$ and $-\langle u'v' \rangle /u_r = 0.00140$ (see fig. 3.23). These values are slightly above the threshold suggested by Ol et al. (2005) and, hence,

---

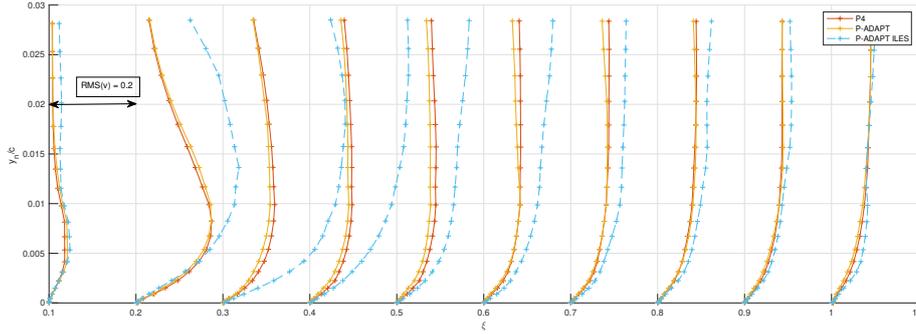[17]This last criterion would be preferable because it does not require an arbitrary choice of the threshold.

Figure 3.22: Comparison between $\mathbb{P}^4$ and $\mathbb{P}$-adaptive LESs and $\mathbb{P}$-adaptive ILES – RMS of y-component of velocity, i.e. $\sqrt{\langle v'^2 \rangle}/u_r$, at chordwise locations $\xi = [0.1, \dots, 1]$ on the suction-side.
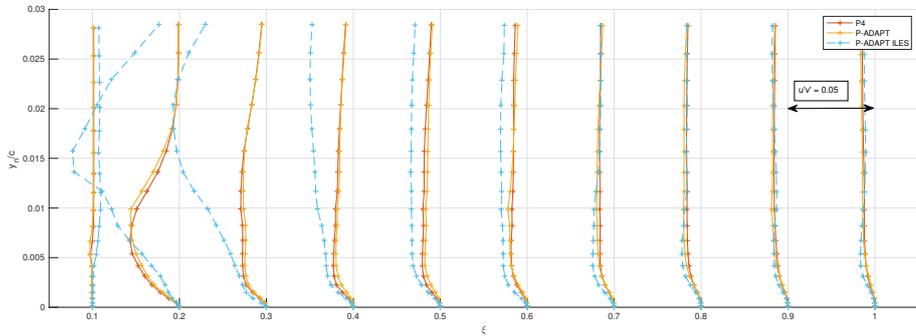

Figure 3.23: Comparison between $\mathbb{P}^4$ and $\mathbb{P}$-adaptive LESs and $\mathbb{P}$-adaptive ILES – Profiles of mean xy-component of Reynolds stresses tensor, i.e. $\langle u'v' \rangle /u_r^2$, at chordwise locations $\xi = [0.1, \dots, 1]$ on the suction-side.

it can be supposed $\xi_t \lesssim 0.1$ for both simulations. Nothing can be said about the transition point of the $\mathbb{P}$-adaptive ILES, other then that it is located between 0.1 and 0.2.

3.4.2 Instantaneous Flow Visualizations

The last comparison between the $\mathbb{P}$-adaptive simulations is shown in fig. 3.24. Once more, the differences between the dimensions of the recirculating region are evident and not negligible.

In fig. 3.25 the instantaneous local Mach number is shown for the $\mathbb{P}$-adaptive LES. The quite high maximum value of 0.41 could justify the higher lift coefficient computed than the ones measured experimentally by Selig (1995) (see again UIUC Wind T. results in table 3.6) [18]. Regarding the influence of the Mach number on the LSB, the experimental results presented by Suwa, Nose, Numata, Nagai, and Asai (2012) for the low Reynolds number flows around a flat plate and a triangular

---

[18]Recall that the increase of the lift coefficient with the Mach number can be explained with the linear potential theory for compressible, inviscid flow. One of the main outcomes of this theory is, indeed, Prandtl–Glauert rule: $C_l = \frac{C_l^{\text{inc.}}}{\sqrt{1-Ma_\infty^2}}$ (see e.g. Anderson, 2010 or Glauert, 1928).
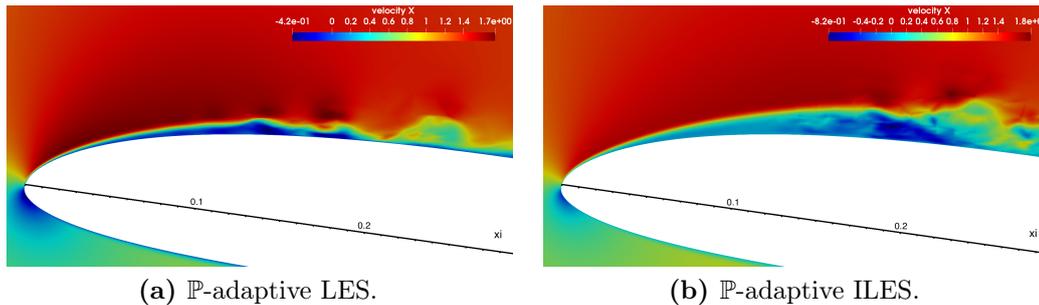
(a) $\mathbb{P}$-adaptive LES.   **(b)** $\mathbb{P}$-adaptive ILES.

Figure 3.24: Comparison between $\mathbb{P}$-adaptive LES with anisotropic model and ILES – Slice for $z = 0.2$ of the instantaneous x-component of the velocity field showing the recirculating region. Note the different velocity scales.
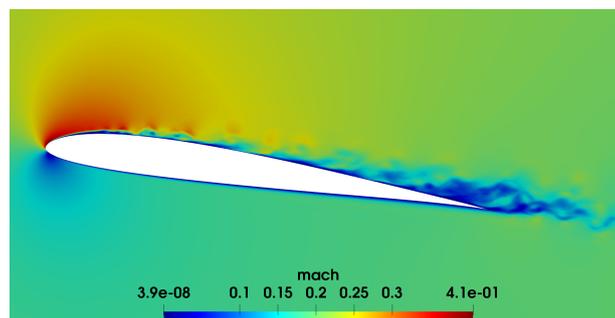

Figure 3.25: Slice for $z = 0.2$ of the instantaneous Mach number obtained with the $\mathbb{P}$-adaptive LES.

airfoil suggest a downstream movement of the LSB with an increase of the Mach number. However it is worth noting that XFOIL predicts the opposite trend for this test case (see again table 3.6). In future works the effect of the Mach number on the LSB will be further investigated.

Thanks to the lower cost of $\mathbb{P}$-adaptive LES (compared to the $\mathbb{P}^4$ simulation), it has been used to investigate the recirculating region. Further comparison with the $\mathbb{P}$-adaptive ILES were not possible due the instability of this simulation.

The visualisation of the instantaneous flow can give an interesting insight into the unsteady flow features. If the steady flow is characterised by a LSB, it is worth noting that the bubble is not visible in the unsteady flow. Indeed it is replaced by a series of large scale vortices which, averaged in time, form the laminar separation bubble. The same conclusion can be found, for example, in the work of Burgmann and Schröder (2008).

Instantaneous pressure iso-surfaces have been used to identify the large scale vortices in the recirculating region. Some attempts have been made also with the Q-criterion but the visualisations were too disturbed to obtain qualitatively interesting results. The noise is due to the velocity derivatives required in the Q-criterion.

Fig. 3.26 shows six instantaneous pressure iso-surfaces corresponding to six consecutive times ($\Delta t = 0.01$) during the $\mathbb{P}$-adaptive simulation. It is possible to observe the generation of a new vortex in the transitional region, the advection and, finally, the decay into small scale structures. The same process has been

observed experimentally by Burgmann and Schröder (2008) and McAuliffe and Yaras (2005) (at $\alpha = 4°$). The high frequency vortex shedding has also an effect on the instantaneous force coefficients, which show a low-amplitude and high-frequency noise.

To estimate the Strouhal number of the vortex shedding, the pressure fluctuations have been recorded every $\Delta t_s = 0.0005$ in the point $(x/c, y/c, z/c) = (0.1354, 0.1756, 0.1)$ for 1 convective time unit. The pressure time history has been windowed using the Hamming function and Fourier-transformed. The resulting Strouhal number based on u_r and L_r have been estimated in the band $19.4 - 22.5$. For a more accurate estimate, a longer observation time should be required. This result is confirmed by fig. 3.27: at $t = t_0$ (fig. 3.26a) the vortex V3 is between $x/c = 0.14$ and $x/c = 0.15$; after 0.05 time units at $t = t_0 + 0.05$ (fig. 3.26f) the vortex V2 is at the same location; this means that, approximately, one period lasts 0.05 time units, i.e. $St \approx 1/0.05 = 20$. The very same observation can be made also for the other vortices. Burgmann and Schröder (2008) reported a vortex frequency of $f = 27.7\,s^{-1}$ measured at $u_\infty = 0.3\,m/s$ and with an airfoil of chord $c = 0.2\,m$. The resulting Strouhal number is $St = \frac{fc}{u_\infty} = 18.47$, which is in a quite good agreement with the one computed in the present work.

3.5 Conclusions

The numerical and experimental results available in literature on the flow around the SD7003 airfoil at $Re = 60\,000$ and $\alpha = 8°$ are quite scattered. For experimental studies, this can be explained with the different background turbulence levels in the facilities. Indeed, it has been proved (see e.g. Herbst et al., 2018) that the T_u has severe influences on the LSB dimensions. For what it concerns numerical results, the (nominally) zero turbulence intensity and the different Mach numbers can only partially explain the differences that can be observed with experimental measurements.

In the present work the dynamic anisotropic model has been used for the closure of the filtered Navier–Stokes equations, leading to a LSB which is much smaller than the majority of the LSBs computed without the SGS model (ILES). This has been explained with the backscatter of energy from the SGS field, which has been proved (see Cimarelli et al., 2019 and Piomelli et al., 1990) to play a key role in the transition to turbulence when a laminar separation, with transition in the free shear layer, is present. As a result, the KH instability is triggered upstream with respect to the ILESs which are not able to capture this phenomenon, leading to a earlier reattachment and a LSB which is closer to experimental measurements.

Furthermore the polynomial adaptivity confirms his capability to capture the flow features with an accuracy comparable with the higher polynomial degree and with a great saving in the computational cost ($\approx 50\%$ of the DOF). Because of that, the $\mathbb{P}$-adaptive approach has been used extensively in chapter 4 to study the blade-vortex interaction starting from the statistically steady state condition computed in the present chapter with the dynamic anisotropic model.

In future works the effects of the Mach number on the force coefficients and on the LSB can be investigated more in depth.
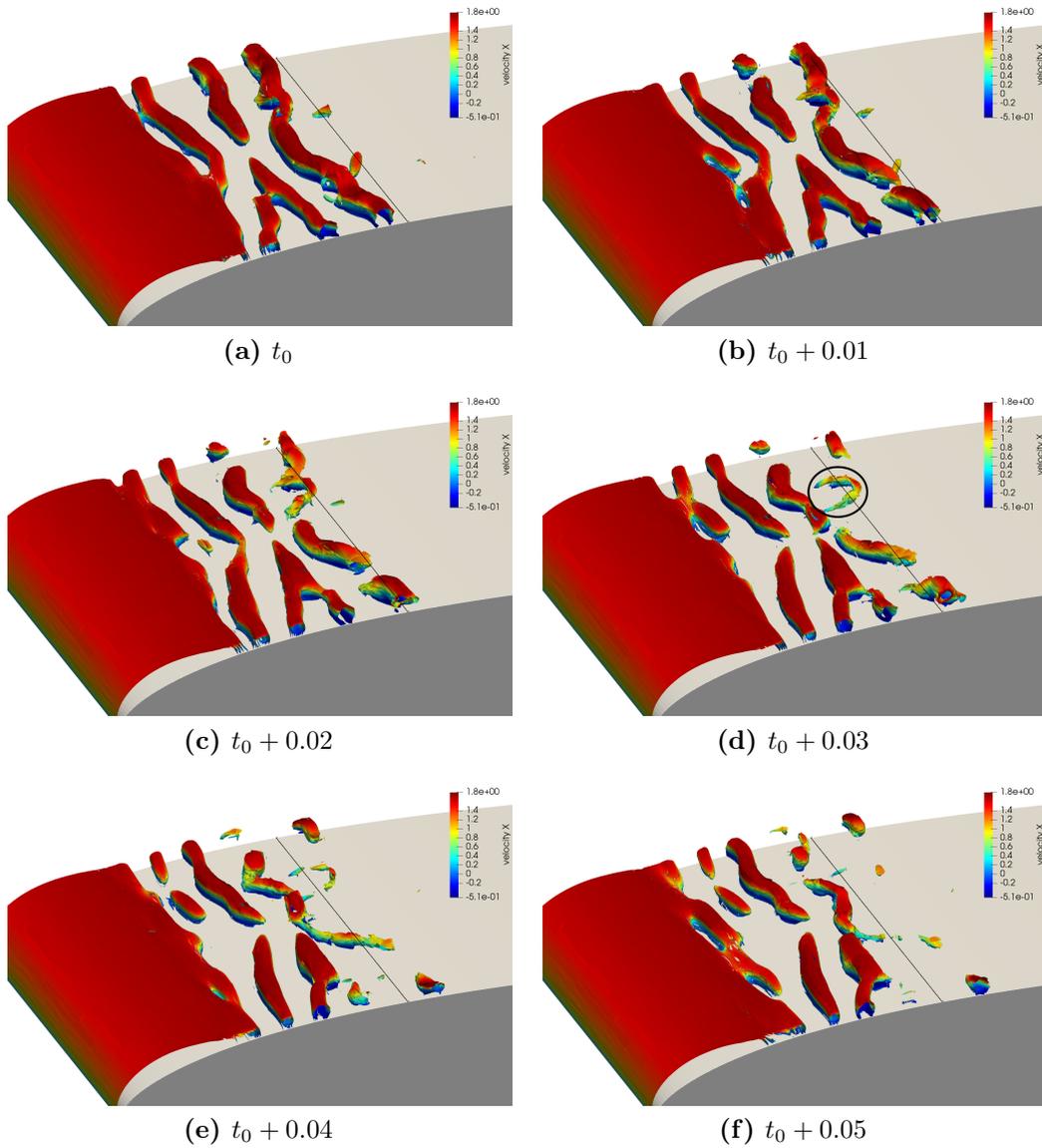
(a) t_0

(b) $t_0 + 0.01$

(c) $t_0 + 0.02$

(d) $t_0 + 0.03$

(e) $t_0 + 0.04$

(f) $t_0 + 0.05$

Figure 3.26: Instantaneous pressure iso-surfaces ($p = 16.89, 16.90, 16.91, 16, 92$) coloured with the x-component of the velocity showing the vortex shedding. They have been obtained with the anisotropic model and p-adaptivity. The black line indicates the mean reattachment line. Note the horseshoe vortex in (d).
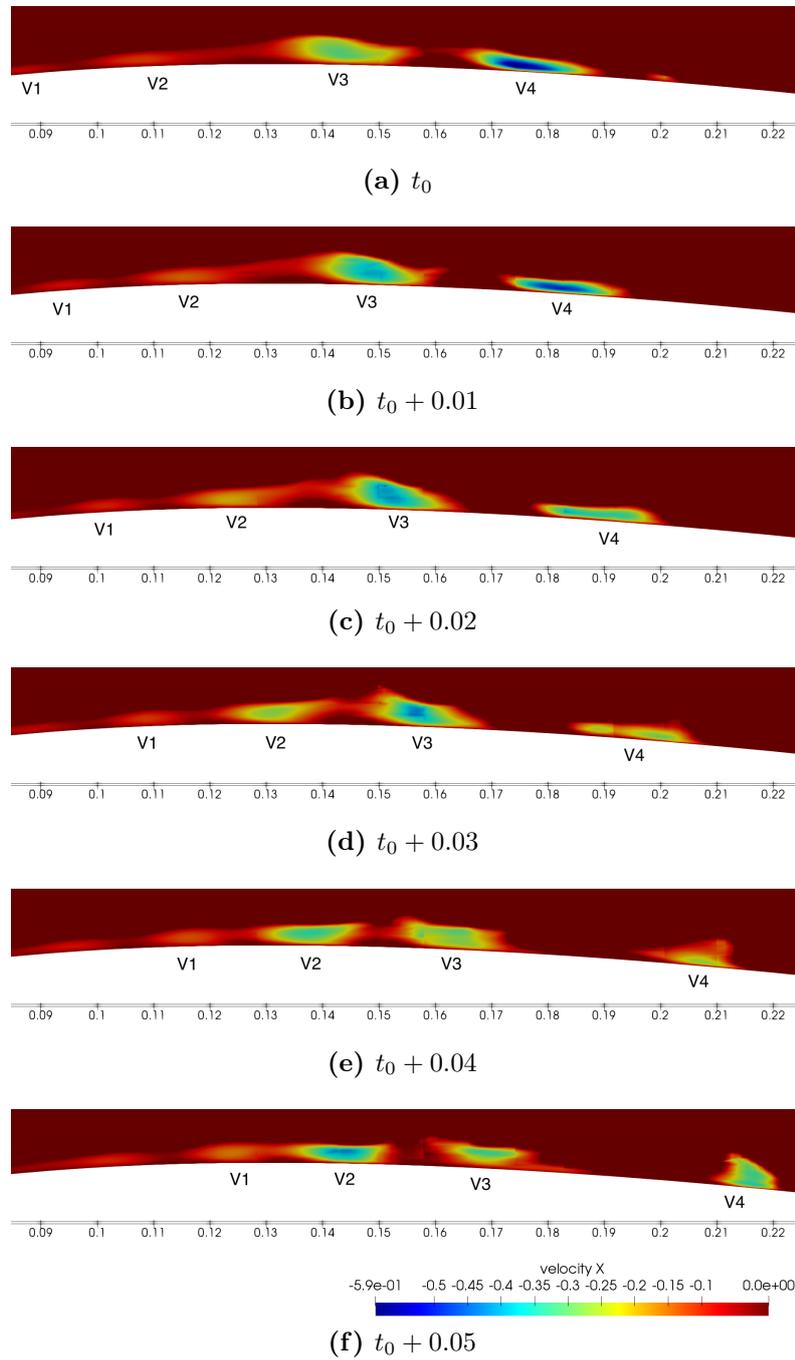
(a) t_0

(b) $t_0 + 0.01$

(c) $t_0 + 0.02$

(d) $t_0 + 0.03$

(e) $t_0 + 0.04$

(f) $t_0 + 0.05$

Figure 3.27: Slice for $z = 0.2$ of the instantaneous x-component of the velocity. Only the negative values are shown to highlight the bottom half of the vortices. They have been obtained with the anisotropic model and p-adaptivity.

Chapter 4

Blade–Vortex Interaction

In this chapter the interaction between a vortex and a SD7003 airfoil at $\alpha = 8°$, $Re = 60\,000$ and $Ma = 0.2$ will be investigated. The axis of the vortex is parallel to the spanwise direction of the airfoil (*parallel* BVI). In literature the type of interaction studied in the present work is usually called *viscous interaction* because of the impact of the vortex viscous core on the leading edge (LE). As a result, the primary vortex splits into two secondary vortices which are advected downstream and, eventually, break down into smaller scales structures (see e.g. Wilder and Telionis, 1998).

The force coefficients during the BVI will be compared with the ones obtained in a reference simulation without the vortex. It will also be investigated the effect of the vortex on the recirculating region which has been studied in chapter 3. As far as the author knowledge, there are not numerical simulation or experimental measurements in literature which can be used for a direct comparison. However some examples of similar works are presented. Felten and Lund (2005) studied the inviscid parallel airfoil(NACA0012)–vortex interaction by means of zonal hybrid RANS/LES method and compared their results with experimental measurements. Ilie et al. (2007) simulate the parallel interaction between a vortex and a NACA0012 airfoil at $\alpha = 0$ and $Re = 1.3 \times 10^6$ using LES with the Smagorinsky model. Experimental studies on parallel BVI on the SD7003 airfoil have been made by Rival et al. (2010) at $Re = 30\,000$; however these results cannot be used for comparison, not only for the different Reynolds number, but, mostly, because two vortices are present in that experimental set-up: one detaches from the trailing edge and the other from the leading edge of an airfoil (vortex generator) collocated upstream to the target airfoil. This configuration is called *Schmidt–propeller configuration*.

In section 4.1 all the details of the simulation are explained, with a particular attention to the vortex model and to the polynomial degree distribution resulting from the $\mathbb{P}$-adaptive approach. In section 4.2 the results are presented and discussed. Finally in section 4.3 the conclusions and some ideas for future works can be found.

4.1 Simulation Set-Up

The BVI simulation has been started from the statistically stationary flow field obtained with the $\mathbb{P}$-adaptive LES (see section 3.2) with the dynamic anisotropic
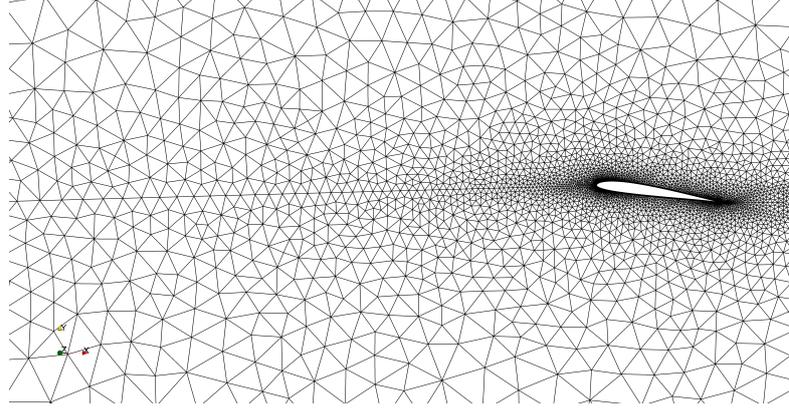
Figure 4.1: Refinement line.

model. The computational domain is the same and it has been described in section 3.1.1 and, as done previously, the ξ-coordinate identifies the chordwise direction. The grid used is the fine mesh described in the same section. The refinement line shown in fig. 4.1 was already present and it was added to prevent the diffusion of the vortex. The maximum characteristic dimension of the tetrahedra along that line is $0.2c$, but, in the region where the vortex has been added, the characteristic dimension of the elements is $\approx 0.1c$. The choice of these values is linked to the characteristic dimension of the vortex which will be discussed later in this section, however it can be anticipated that the vortex core diameter is $0.1c$. Exploiting the results of Tugnoli (2017) and Tugnoli, Abbà, and Bonaventura (2019), a characteristic element dimension comparable to the core diameter has been used, since it is sufficient to prevent the diffusion of the vortex with a $\mathbb{P}^4$ degree.

The time step is the same of the $\mathbb{P}$-adaptive simulation of section 3.2 ($\Delta t = 1.1 \times 10^{-5}$) and also the boundary conditions presented in section 3.1.2 are unchanged.

The definition of the (modelled) vortex is the one proposed by Lodato, Domingo, and Vervisch (2008) and it is formulated in terms of stream function Ψ:

$$\Psi = C_v \, \exp\left(-\frac{r^2}{2R_v^2}\right) \tag{4.1}$$

where C_v is the vortex strength, $r^2 = (x - x_v)^2 + (y - y_v)^2$ is the distance from the vortex centre $(x_v/c, y_v/c)$ and R_v is the vortex core radius. The velocity induced by the vortex is:

$$u = \frac{\partial \Psi}{\partial x} = -C_v \frac{y}{R_v^2} \, \exp\left(-\frac{r^2}{2R_v^2}\right) \tag{4.2}$$

$$v = -\frac{\partial \Psi}{\partial y} = C_v \frac{x}{R_v^2} \, \exp\left(-\frac{r^2}{2R_v^2}\right) \tag{4.3}$$

$$w = 0 \tag{4.4}$$

in the xyz reference frame and

$$u_r = \frac{1}{r}\frac{\partial \Psi}{\partial \theta} = 0 \tag{4.5}$$

$$u_\theta = -\frac{\partial \Psi}{\partial r} = C_v \frac{r}{R_v^2}\,\exp\left(-\frac{r^2}{2R_v^2}\right) \tag{4.6}$$

$$w = 0 \tag{4.7}$$

in a cylindrical reference frame. In both reference frames the z-axis is centred in the vortex centre. The maximum tangential velocity is $u_{\theta,\mathrm{max}} = C_v/(R_v\sqrt{e})$ at $r = R_v$. The pressure radial distribution has been modelled as done by Colonius, Lele, and Moin (1991) for a compressible viscous vortex:

$$\frac{\partial p}{\partial r} = \frac{\rho u_\theta^2}{r}. \tag{4.8}$$

Assuming that the temperature T does not change because of the vortex superimposition, one should obtain:

$$p = p_{\mathrm{old}}\,\exp\left[-\frac{C_v^2}{2TR_v^2}\exp\left(-\frac{r^2}{R_v^2}\right)\right], \tag{4.9}$$

with p_{old} the pressure of the statistically steady-state initial condition. Finally the density is:

$$\rho = \frac{p}{T} \tag{4.10}$$

Recall that all the quantities have been made dimensionless with unitary reference values L_r, ρ_r, u_r, T_r and $p_r = \rho_r R_{\mathrm{gas}} T_r$[1].

The vortex has been superimposed to the statistically steady flow field in $(x_v/c, y_v/c) = (-1, -0.0166)$, i.e. one chord upstream to the leading edge (LE) and slightly below the trailing edge (TE). Because of the velocity induced by the airfoil, from this position, the vortex hits the LE. It has been verified (see section 4.2) that one chord upstream is sufficient to avoid any initial influences on the airfoil coming from the vortex superimposition. The vortex radius chosen is $R_v = 0.05$, which is comparable with the experimental measurements of Droandi et al. (2016), Zanotti, Ermacora, Campanardi, and Gibertini (2014) and Steinhoff and Raviprakash (1995). The vortex strength C_v has been computed from the maximum tangential velocity $u_{\theta,\mathrm{max}} = 0.5$ measured in the aforementioned works of Droandi et al. (2016) and Zanotti et al. (2014). The resulting value is $C_v = u_{\theta,\mathrm{max}} R_v \sqrt{e} \approx 0.0412$. The vortex rotates in the counter-clockwise direction. In fig. 4.2 the radial distributions for tangential velocity, density and pressure are shown.

For this simulation the dynamic p-adaption have been used to better represent the unsteady BVI phenomenon. The thresholds for the choice of the polynomial degree have been kept equal to the ones used to reach the statistically steady-state condition: $\epsilon_1 = 1.0 \times 10^{-4}$ and $\epsilon_2 = 1.0 \times 10^{-2}$. The SF indicator has been computed every 4 time steps ($\Delta t_{\mathrm{ind}} = 4.4 \times 10^{-5}$) and averaged over 30 evaluations before the

---

[1]Actually, all the quantities are the filtered ones. The filter operator has been omitted here to make the notation simpler.
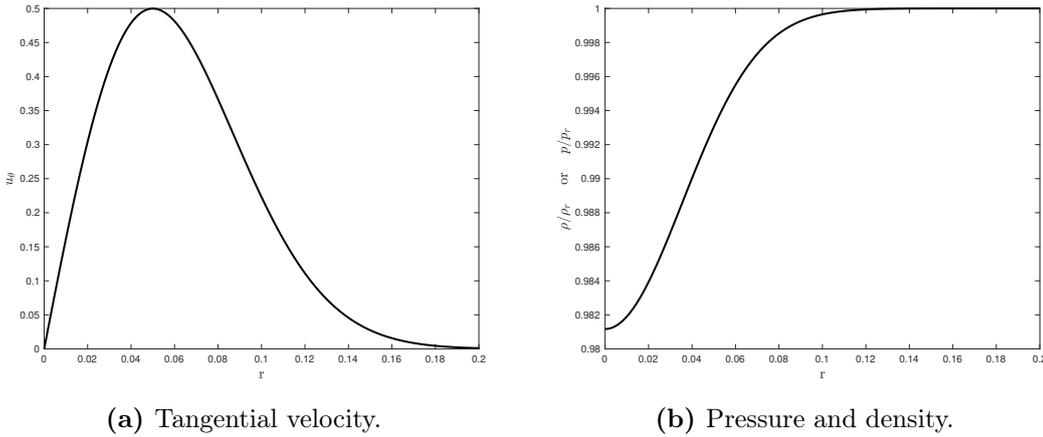
(a) Tangential velocity.

(b) Pressure and density.

Figure 4.2: Tangential velocity, pressure and density radial distributions for the vortex model. In (b) it has been assumed $p_{\mathrm{old}} = p_r$.

actual adaption ($\Delta t_{\mathrm{adapt}} = 30\,\Delta t_{\mathrm{ind}} = 1.32 \times 10^{-3}$). These time intervals ensure to accurately follow the vortex advection which moves at $u_{\mathrm{vort}} \approx u_r = 1$ and to average the indicator on a number of samples statistically meaningful. Furthermore the adaption frequency $f_{\mathrm{adapt}} = 1/\Delta t_{\mathrm{adapt}} \approx 758$ is also much higher than the vortex shedding frequency (Strouhal) in the recirculating region ($St \approx 20$, see section 3.4.2): in this way also this unsteady phenomenon is correctly represented by the dynamic adaption technique.

Some examples of the resulting polynomial degree distribution are shown in fig. 4.3 for different time instants (the vortex has been introduced at $t = 0$). The SF indicator is able to detect the vortex and, thanks to the dynamic adaption technique, it is also able to follow his advection during time. After the impact of the primary vortex on the TE of the airfoil (figs. 4.3c and 4.3d) the SF indicator detects accurately the position of the two secondary vortices. Thanks to the threshold chosen, the fourth order degree is used in the vortex core, as shown in fig. 4.4a. This prevents the over-diffusion of the vortex during its advection, before the actual interaction with the airfoil (see Tugnoli, 2017). It is worth noting that a fourth order polynomial degree is used also for the secondary vortex on the pressure side (see fig. 4.4b).

4.2 BVI Results and Discussion

From an engineering point of view, one of the most interesting result is the amplitude in the loads oscillation for structural analysis. The force coefficients have been recorded for 2 convective time units after the introduction of the vortex. They are compared in fig. 4.5 with a reference $\mathbb{P}$-adaptive simulation without the vortex. The details of the reference simulation can be found in section 3.2. The moment coefficient has been computed with respect to the quarter of chord and positive clockwise, as done in chapter 3. Until $t \approx 0.6$, i.e. until the vortex is $\approx 0.4c$ upstream the airfoil, the force coefficients do not significantly deviate from the
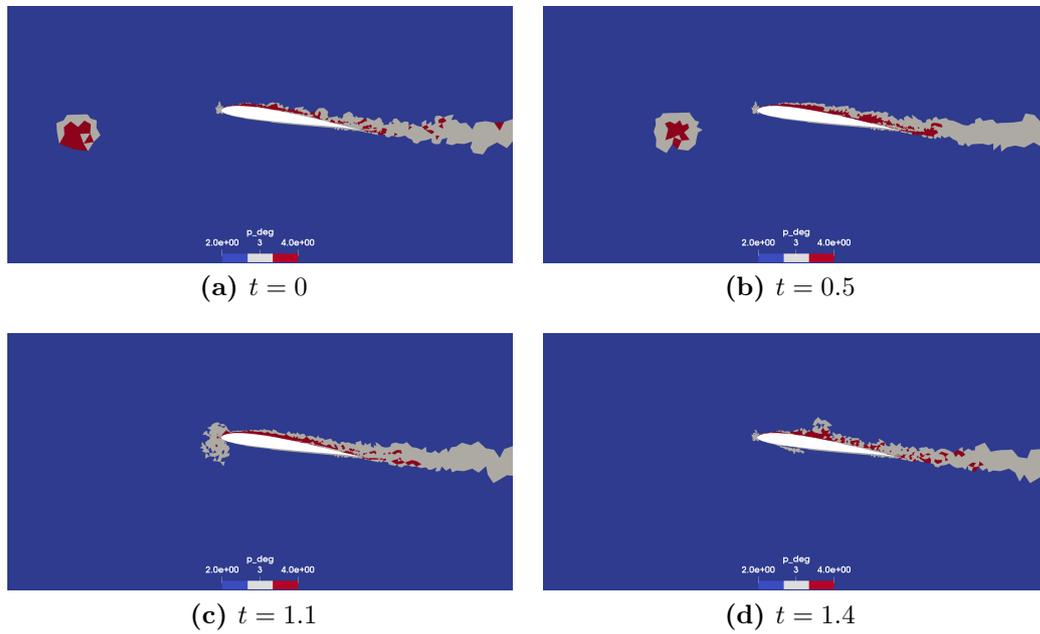
(a) $t = 0$

(b) $t = 0.5$

(c) $t = 1.1$

(d) $t = 1.4$

Figure 4.3: 2D view ($z = 0.2$) of the polynomial degree distribution at different instants.

(a) $t = 0$ – Suction side

(b) $t = 1.4$ – Pressure side
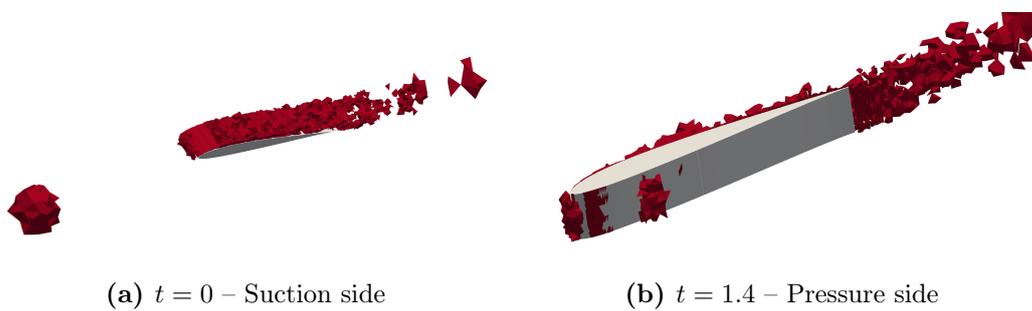
Figure 4.4: Elements in which a 4th order polynomial is used at different instants.

(a) Lift coefficient

(b) Drag coefficient

(c) Moment coefficient
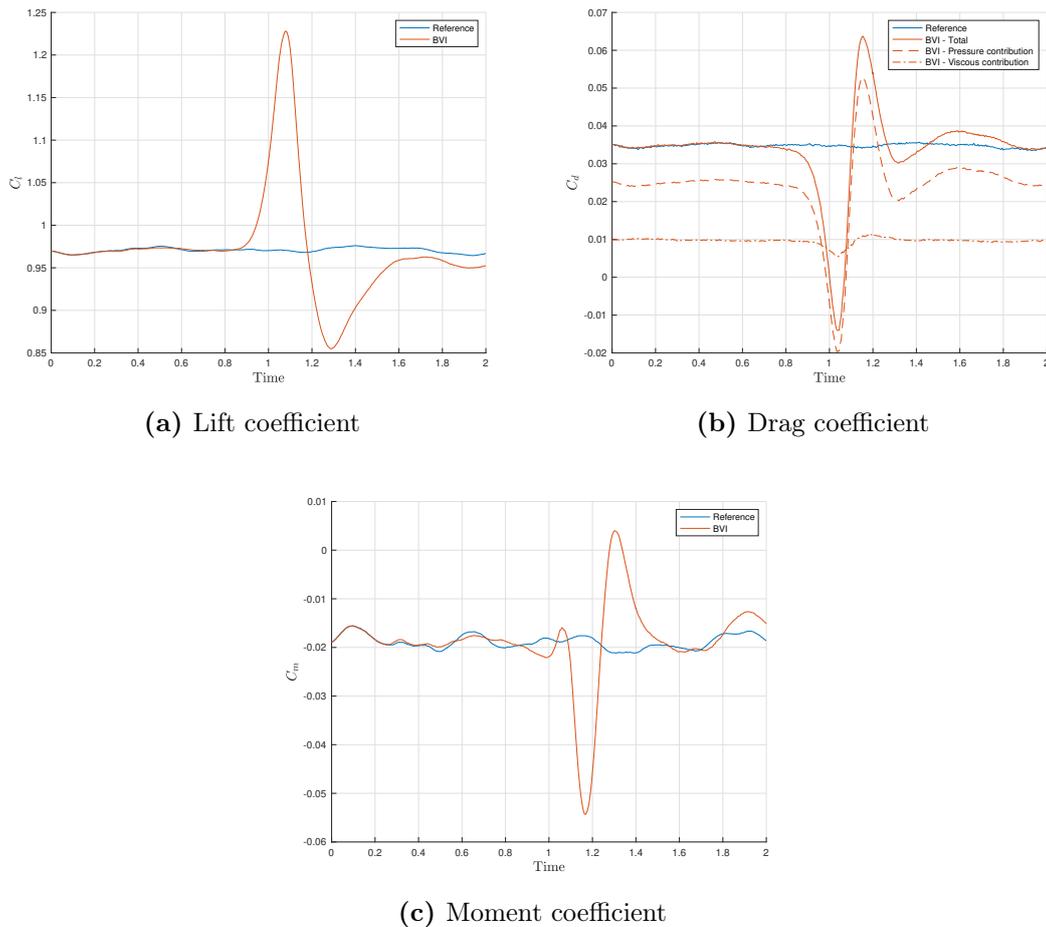
Figure 4.5: Force coefficients during the BVI compared with a reference simulation without the vortex.

reference simulation: this means that the initial position of the vortex is sufficiently far from the airfoil to correctly simulate the BVI. The differences in the coefficients until $t \approx 0.6$ are probably due to the different $\mathbb{P}$-adaptive approach of the two simulations (*static* adaptivity for the reference simulation and *dynamic* adaptivity for the BVI simulation, see section 2.4).

The drag is the first component of the aerodynamic force to change because of the presence of the vortex. It decreases and reaches its minimum value of $C_{d,\min} = -0.014$ at $t = 1.04$: the airfoil is pulled by the low pressure core of the vortex. This is confirmed by the fact that the stronger variation in the drag is pressure-driven (fig. 4.5b). On the other hand the lift increases because the vortex is rotating counter-clockwise and, hence, it induces a higher angle of attack on the airfoil. The maximum value of the lift coefficient is $C_{l,\max} = 1.228$ (+27% of its mean value of 0.9693) at $t = 1.08$. Differently on what one could expect, the minimum value of the moment coefficient is slightly delayed with respect to the instant of maximum lift: the aerodynamic moment reaches its minimum value of $C_{m,\min} = -0.054$ (+190% of its mean value of -0.0186) at $t = 1.17$. The reason of this fact is not trivial, since between $t \approx 1$ and $t \approx 1.2$ several different phenomena
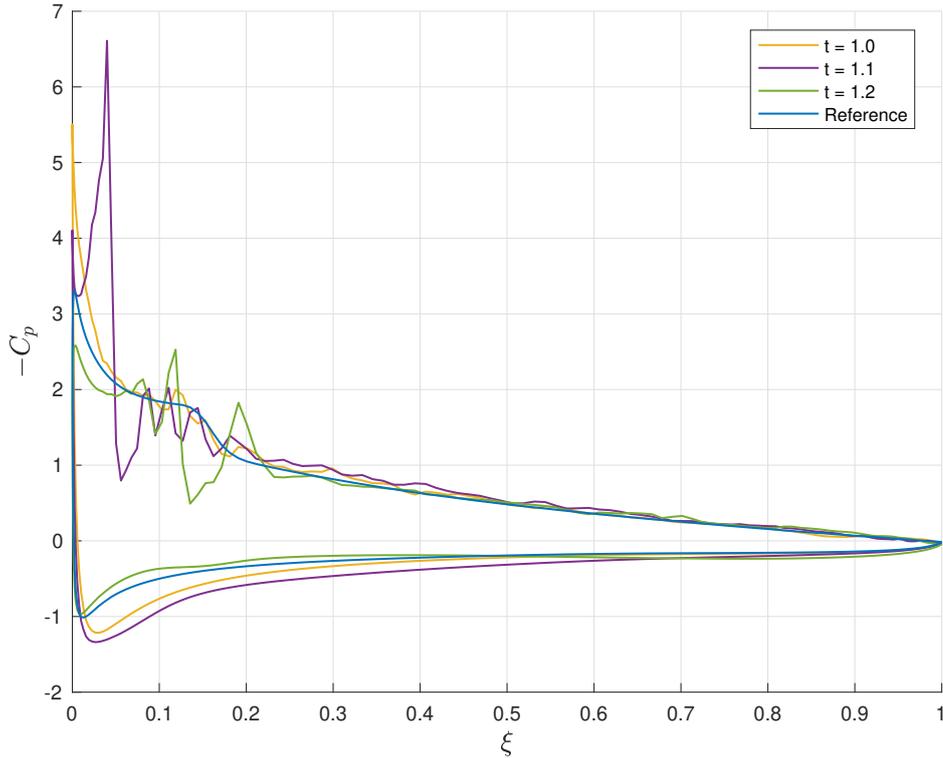
Figure 4.6: Pressure coefficient at different instants compared with the reference (statistically steady-state) simulation.

occur almost simultaneously; however a possible explanation is given here.

First of all, when the vortex moves closer, the induced angle of attack changes the pressure distribution mainly for $0 < \xi \lesssim 0.2$ in both the pressure and suction-side (see fig. 4.6, $t = 1.0$ curve); this results in an increase in the lift coefficient. After hitting the LE at $t = 1.04$ (minimum drag instant), the vortex splits in two: on the suction-side the low pressure core causes the peak clearly visible on the pressure distribution in fig. 4.6 ($t = 1.1$ curve); on the pressure-side the secondary vortex has not started being advected on the surface yet and, hence, the pressure is still higher than its the steady state value. On the suction-side, after the passage of the secondary vortex, the pressure is significantly higher than the steady-state reference condition, especially for $0 < \xi \lesssim 0.3$ (fig. 4.6, $t = 1.2$ curve); this results in the decrease of the moment coefficient which reaches its minimum value. Furthermore this effect is accentuated by the pressure distribution on the pressure-side: the low pressure core of the secondary vortex at $\xi \approx 0.1$ and the higher pressure for $\xi > 0.5$ (see again $t = 1.2$ curve of fig. 4.6) lower even more the moment coefficient. The higher pressure for $\xi > 0.5$ is caused by the acoustic wave resulting from the impact of the vortex on the LE (see fig. 4.9b). While the lift coefficient is overall reduced, the drag coefficient reaches its maximum value of $C_{d,\max} = 0.064$ (+85% of its mean value of 0.0346) at $t = 1.15$, mainly because of the change in the pressure contribution (see fig. 4.5b).

After $t = 1.2$ the lift continues to decrease until $t = 1.3$ causing a positive peak

in the moment coefficient $C_{m,\max} = 0.004$ for the same instant. This is probably due to a small separation induced by the secondary vortex on the suction-side. It is worth noting that during the last time instants the drag coefficient reaches the steady-state value, while the lift is still lower (consequently the moment coefficient is higher). A longer simulation would be required to observe the end of the transient.

The effect of the passage of the vortex on the recirculating region on the suction-side is show in fig. 4.7. It is worth noting a "2D regularisation" of the small vortices (figs. 4.7b to 4.7f) while the superimposed vortex approaches. This is due to the two-dimensional nature of the superimposed vortex. The vortex which causes the low pressure peak in the C_p at $t = 1.1$ is clearly visible in fig. 4.7f. After the passage of the vortex (fig. 4.7i) the recirculating region changes greatly, affecting lift and moment coefficients: the vortex shedding of the statistically steady-state condition is no longer present (fig. 4.7j). Also at the last time instant recorded ($t = 2$), the vortices are smaller, less intense and at lower frequency (fig. 4.8b) if compared to the instants before the interaction (fig. 4.7b) or to the reference simulation (fig. 3.26 in the previous chapter).

Another interesting quantity to be analysed during the BVI is the pressure perturbation far from the airfoil for an aeroacoustic analysis: when the vortex hits the LE an acoustic (pressure) wave departs from that point. For this type of study, a much more resolved mesh is required to prevent the over-dissipation of the acoustic wave and it goes beyond the scope of the present work. However, also with the grid used, the pressure wave has been detected and it is show in fig. 4.9 by means of pressure perturbation. It is worth noting that for $t = 1.2$ (fig. 4.9b) the acoustic wave influences the pressure distribution on the pressure-side (see again $t = 1.2$ curve of fig. 4.6): as explained previously, the pressure is increased for $\xi > 0.5$ because of the pressure wave, contributing to the lowering of the moment coefficient. A quantitative analysis of the sound pressure level has not been done.

4.3   Conclusions and Future Perspectives

The parallel, viscous BVI has been studied using the dynamic $\mathbb{P}$-adaptive approach in a DG framework. The results are compared with a reference static $\mathbb{P}$-adaptive simulation validated in chapter 3 to show the effects of the interaction on the aerodynamic forces. Lift, drag and moment coefficients are all affected by this interaction. It has been noticed that the transient of the lift and moment coefficients is longer than the one of the drag which rapidly comes back to the statistically steady-state condition. This has been explained with the less intense vortex shedding phenomenon in the recirculating region which persists over time after the BVI, affecting the lift and moment coefficients.

In future works it could be interesting to investigate different vortex positions (i.e. inviscid interaction), rotation directions and angles of attack of the airfoil to find the most critical condition. Furthermore, using a more refined mesh and a wider domain, an aeroacoustic analysis could be done.
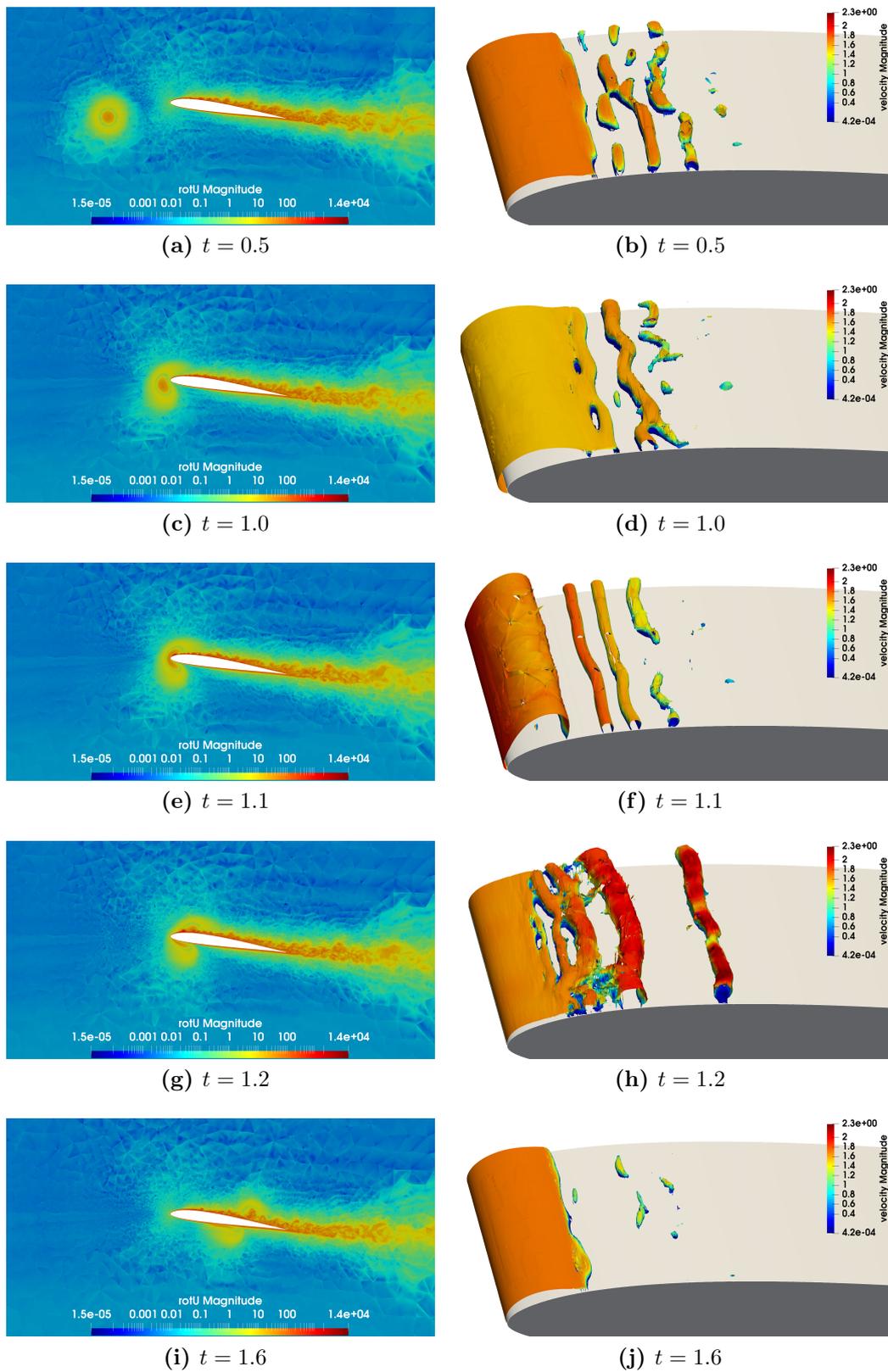
(a) $t = 0.5$

(b) $t = 0.5$

(c) $t = 1.0$

(d) $t = 1.0$

(e) $t = 1.1$

(f) $t = 1.1$

(g) $t = 1.2$

(h) $t = 1.2$

(i) $t = 1.6$

(j) $t = 1.6$

Figure 4.7: Continues in fig. 4.8, see there for the caption.

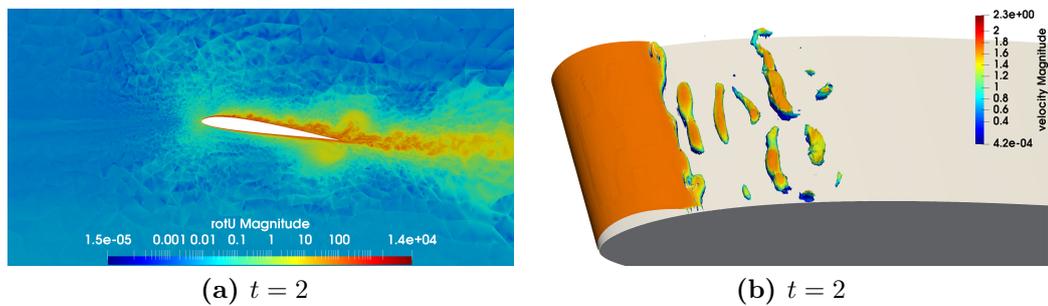(a) $t = 2$ (b) $t = 2$

Figure 4.8: Left: 2D view ($z = 0.2$) of the vorticity magnitude in logarithmic scale. Right: instantaneous pressure iso-surfaces ($p = 16.89, 16.90, 16.91, 16, 92$) coloured with the velocity magnitude.
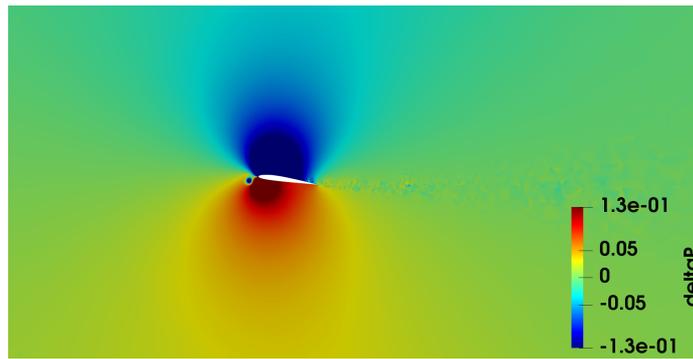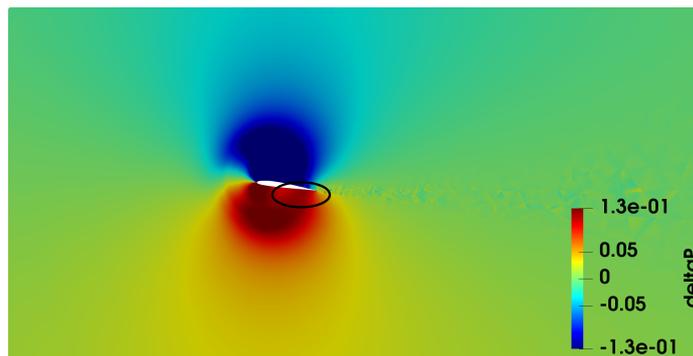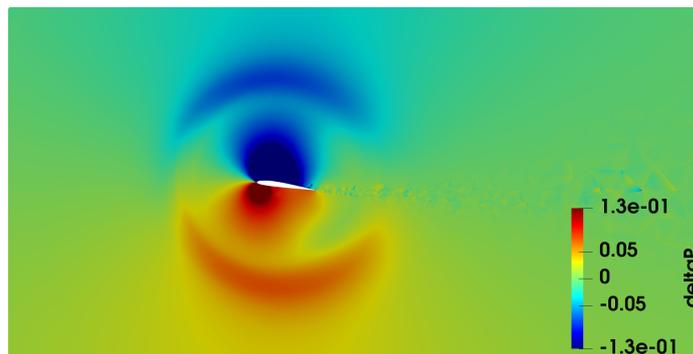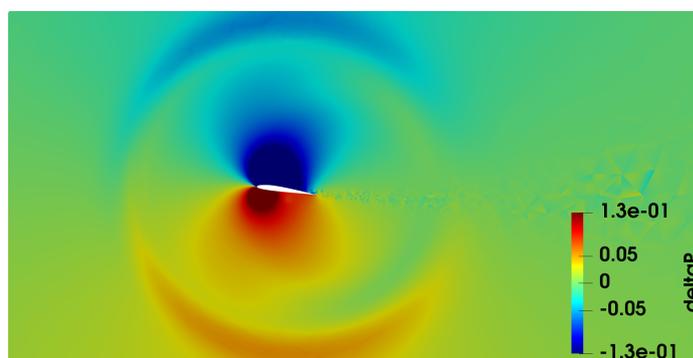
(a) $t = 0.9$

(b) $t = 1.2$

(c) $t = 1.4$

(d) $t = 1.6$

Figure 4.9: Slice for $z = 0.2$ of pressure perturbation $p - p_r$ at different time instants. Note in (b) that the acoustic wave influences the pressure (C_p) distribution on the pressure-side.

Bibliography

Abbà, A., Bonaventura, L., Nini, M., & Restelli, M. (2015). Dynamic models for large eddy simulation of compressible flows with a high order DG method. *Computers & Fluids, 122*, 209–222. doi:https://doi.org/10.1016/j.compfluid.2015.08.021

Abbà, A., Bonaventura, L., Recanati, A., & Tugnoli, M. (2019). Dynamical p-adaptivity for les of compressible flows in a high order dg framework. arXiv: 1911.01241 [physics.flu-dyn]

Abbà, A., Campaniello, D., & Nini, M. (2017). Filter size definition in anisotropic subgrid models for large eddy simulation on irregular grids. *Journal of Turbulence, 18*(6), 589–610. doi:10.1080/14685248.2017.1312001. eprint: https://doi.org/10.1080/14685248.2017.1312001

Abbà, A., Cercignani, A., & Valdettaro, L. (2003). Analysis of subgrid scale models. *Computers and Mathematics with Applications, 46*(4), 521–535. Turbulence Modelling and Simulation. doi:https://doi.org/10.1016/S0898-1221(03)90014-9

Abbà, A., Cercignani, C., Picarella, G., & Valdettaro, L. (2001). A 3d turbulent boundary layer test for LES models. In *Computational fluid dynamics 2000* (pp. 485–490). Springer.

Abdalla, I. E., & Yang, Z. (2004). Numerical study of the instability mechanism in transitional separating–reattaching flow. *International Journal of Heat and Fluid Flow, 25*(4), 593–605. doi:https://doi.org/10.1016/j.ijheatfluidflow.2004.01.004

Alam, M., & Sandham, N. D. (2000). Direct numerical simulation of 'short' laminar separation bubbles with turbulent reattachment. *Journal of Fluid Mechanics, 410*, 1–28. doi:10.1017/S0022112099008976

Anderson, J. (2010). *Fundamentals of aerodynamics*. McGraw-Hill Education. Retrieved from https://books.google.it/books?id=xwY8PgAACAAJ

Bassi, F., Botti, L., Colombo, A., Crivellini, A., Ghidoni, A., & Massa, F. (2016). On the development of an implicit high-order discontinuous galerkin method for DNS and implicit LES of turbulent flows. *European Journal of Mechanics - B/Fluids, 55*, 367–379. Vortical Structures and Wall Turbulence. doi:https://doi.org/10.1016/j.euromechflu.2015.08.010

Bassi, F., Colombo, A., Crivellini, A., Fidkowski, K., Franciolini, M., Ghidoni, A., & Noventa, G. (2019). An entropy-adjoint p-adaptive discontinuous galerkin method for the under-resolved simulation of turbulent flows. In *Aiaa aviation 2019 forum*. doi:10.2514/6.2019-3418. eprint: https://arc.aiaa.org/doi/pdf/10.2514/6.2019-3418

Bassi, F., & Rebay, S. (1997). A high-order accurate discontinuous finite element method for the numerical solution of the compressible navier–stokes equations. *Journal of Computational Physics*, *131*(2), 267–279. doi:https://doi.org/10.1006/jcph.1996.5572

Bernardos, L., Richez, F., Gleize, V., & Gerolymos, G. A. (2019). Prediction of separation-induced transition on the sd7003 airfoil using algebraic transition triggering. *AIAA Journal*, *57*(9), 3812–3824. doi:10.2514/1.J058288. eprint: https://doi.org/10.2514/1.J058288

Bolemann, T., Beck, A., Flad, D., Frank, H., Mayer, V., & Munz, C. .-.-D. (2015). High-order discontinuous galerkin schemes for large-eddy simulations of moderate reynolds number flows. In N. Kroll, C. Hirsch, F. Bassi, C. Johnston, & K. Hillewaert (Eds.), *Idihom: Industrialization of high-order methods - a top-down approach: Results of a collaborative research project funded by the european union, 2010 - 2014* (pp. 435–456). doi:10.1007/978-3-319-12886-3_20

Boom, P., & Zingg, D. (2013). Time-accurate flow simulations using an efficient newton-krylov-schur approach with high-order temporal and spatial discretization. doi:10.2514/6.2013-383

Breuer, M. (2018). Effect of inflow turbulence on an airfoil flow with laminar separation bubble: An les study. *Flow, Turbulence and Combustion*, *101*(2), 433–456. doi:10.1007/s10494-017-9890-2

Burgmann, S., & Schröder, W. (2008). Investigation of the vortex induced unsteadiness of a separation bubble via time-resolved and scanning piv measurements. *Experiments in Fluids*, *45*, 675–691. doi:10.1007/s00348-008-0548-7

Catalano, P., & Tognaccini, R. (2009). Influence of free-stream turbulence on simulations of laminar separation bubbles. In *47th aiaa aerospace sciences meeting including the new horizons forum and aerospace exposition*. doi:10.2514/6.2009-1471. eprint: https://arc.aiaa.org/doi/pdf/10.2514/6.2009-1471

Catalano, P., & Tognaccini, R. (2010). Turbulence modeling for low-reynolds-number flows. *AIAA Journal*, *48*(8), 1673–1685. doi:10.2514/1.J050067. eprint: https://doi.org/10.2514/1.J050067

Catalano, P., & Tognaccini, R. (2011). Rans analysis of the low-reynolds number flow around the sd7003 airfoil. *Aerospace Science and Technology*, *15*(8), 615–626. doi:https://doi.org/10.1016/j.ast.2010.12.006

Cimarelli, A., Leonforte, A., De Angelis, E., Crivellini, A., & Angeli, D. (2019). Resolved dynamics and subgrid stresses in separating and reattaching flows. *Physics of Fluids*, *31*(9), 095101. doi:10.1063/1.5110036. eprint: https://doi.org/10.1063/1.5110036

Cockburn, B., & Shu, C.-W. (1998). The local discontinuous galerkin method for time-dependent convection-diffusion systems. *SIAM Journal on Numerical Analysis*, *35*(6), 2440–2463. doi:10.1137/S0036142997316712. eprint: https://doi.org/10.1137/S0036142997316712

Colonius, T., Lele, S. K., & Moin, P. (1991). The free compressible viscous vortex. *Journal of Fluid Mechanics*, *230*, 45–73. doi:10.1017/S0022112091000708

Crivellini, A. (2016). Assessment of a sponge layer as a non-reflective boundary treatment with highly accurate gust–airfoil interaction results. *International Journal of Computational Fluid Dynamics*, *30*(2), 176–200. doi:10.1080/

10618562.2016.1167193. eprint: https://doi.org/10.1080/10618562.2016.1167193

Drela, M. (1989). Xfoil: An analysis and design system for low reynolds number airfoils. In T. J. Mueller (Ed.), *Low reynolds number aerodynamics* (pp. 1–12). Berlin, Heidelberg: Springer Berlin Heidelberg.

Droandi, G., Gibertini, G., & Zanotti, A. (2016). Perpendicular blade–vortex-interaction over an oscillating airfoil in light dynamic stall. *Journal of Fluids and Structures*, *65*, 472–494. doi:https://doi.org/10.1016/j.jfluidstructs.2016.07.010

Ducoin, A., Loiseau, J.-C., & Robinet, J.-C. (2015). Direct Numerical Simulation of the laminar to turbulent transition on a hydrofoil. In *Fourth International Symposium on Marine Propulsors, smp'15, , Texas, USA, June 2015*, Austin, United States. Retrieved from https://hal.archives-ouvertes.fr/hal-01194767

Eidson, T. (1985). Numerical simulation of the turbulent Rayleigh-Bénard problem using subgrid modelling. *Journal of Fluid Mechanics*, *158*, 245–268. cited By 108. doi:10.1017/S0022112085002634

Erlebacher, G., Hussaini, M. Y., Speziale, C. G., & Zang, T. A. (1992). Toward the large-eddy simulation of compressible turbulent flows. *Journal of Fluid Mechanics*, *238*, 155–185. doi:10.1017/S0022112092001678

Felten, F., & Lund, T. (2005). Numerical simulation of parallel airfoil/vortex interaction using a zonal hybrid RANS/LES method. (Vol. 5127). doi:10.2514/6.2005-5127

Galbraith, M., & Visbal, M. (2008). Implicit large eddy simulation of low reynolds number flow past the sd7003 airfoil. (Vol. 225). doi:10.2514/6.2008-225

Garmann, D. J., Visbal, M. R., & Orkwis, P. D. (2013). Comparative study of implicit and subgrid-scale model large-eddy simulation techniques for low-reynolds number airfoil applications. *International Journal for Numerical Methods in Fluids*, *71*(12), 1546–1565. doi:10.1002/fld.3725. eprint: https://onlinelibrary.wiley.com/doi/pdf/10.1002/fld.3725

Germano, M. (1992). Turbulence: The filtering approach. *Journal of Fluid Mechanics*, *238*, 325–336.

Germano, M., Piomelli, U., Moin, P., & Cabot, W. H. (1991). A dynamic subgrid-scale eddy viscosity model. *Physics of Fluids A: Fluid Dynamics*, *3*(7), 1760–1765.

Gibertini, G., Abbà, A., Auteri, F., & Belan, M. (2010). Flow around two in-tandem flat plates: Measurements and computations comparison. In *5th international conference on vortex flows and vortex models (icvfm2010)* (pp. 1–8).

Glauert, H. (1928). The effect of compressibility on the lift of an aerofoil. *Proceedings of the Royal Society of London. Series A, Containing Papers of a Mathematical and Physical Character*, *118*(779), 113–119. Retrieved from http://www.jstor.org/stable/94892

Hain, R., Kahler, C. J., & Radespiel, R. (2009). Dynamics of laminar separation bubbles at low-reynolds-number aerofoils. *Journal of Fluid Mechanics*, *630*, 129–153. doi:10.1017/S0022112009006661

Herbst, S. L., Kähler, C. J., & Hain, R. (2018). Influence of large-scale free-stream turbulence on an sd7003 airfoil at low reynolds numbers. In *2018*

applied aerodynamics conference. doi:10.2514/6.2018-3490. eprint: https://arc.aiaa.org/doi/pdf/10.2514/6.2018-3490

Ilie, M. (2019). A fully-coupled CFD/CSD computational approach for aeroelastic studies of helicopter blade-vortex interaction. *Applied Mathematics and Computation, 347,* 122–142. doi:10.1016/j.amc.2018.10.069

Ilie, M., Nitzche, F., & Matida, E. (2007). Two-dimensional blade-vortex interaction using large eddy simulation. In *48th AIAA/ASME/ASCE/AHS/ASC structures, structural dynamics, and materials conference.* doi:10.2514/6.2007-2066. eprint: https://arc.aiaa.org/doi/pdf/10.2514/6.2007-2066

Karypis, G., & Kumar, V. (1998). A fast and high quality multilevel scheme for partitioning irregular graphs. *SIAM Journal on Scientific Computing, 20*(1), 359–392. doi:10.1137/S1064827595287997. eprint: https://doi.org/10.1137/S1064827595287997

Kompenhans, M., Rubio, G., Ferrer, E., & Valero, E. (2016). Comparisons of p-adaptation strategies based on truncation- and discretisation-errors for high order discontinuous galerkin methods. *Computers & Fluids, 139,* 36–46. 13th USNCCM International Symposium of High-Order Methods for Computational Fluid Dynamics - A special issue dedicated to the 60th birthday of Professor David Kopriva. doi:https://doi.org/10.1016/j.compfluid.2016.03.026

Lodato, G., Domingo, P., & Vervisch, L. (2008). Three-dimensional boundary conditions for direct and large-eddy simulation of compressible viscous flows. *Journal of Computational Physics, 227*(10), 5105–5143. doi:https://doi.org/10.1016/j.jcp.2008.01.038

McAuliffe, B. R., & Yaras, M. I. (2005). Separation-Bubble-Transition Measurements on a Low-Re Airfoil Using Particle Image Velocimetry, *Volume 3: Turbo Expo 2005, Parts A and B,* 1029–1038. doi:10.1115/GT2005-68663. eprint: https://asmedigitalcollection.asme.org/GT/proceedings-pdf/GT2005/47268/1029/2638263/1029_1.pdf

Morvant, R., Badcock, K. K., & Barakos, G. G. (2005). Aerofoil-vortex interaction using the compressible vorticity confinement method. *AIAA Journal, 43*(1), 63–75. doi:10.2514/1.5177. eprint: https://doi.org/10.2514/1.5177

Naddei, F. (2019). *Adaptive large eddy simulations based on discontinuous galerkin methods* (PhD Thesis, Université Paris-Saclay).

Naddei, F., de la Llave Plata, M., & Couaillier, V. (2018). A comparison of refinement indicators for p-adaptive discontinuous galerkin methods for the euler and navier-stokes equations. doi:10.2514/6.2018-0368

Nobach, H., & Tropea, C. (2007). Fundamentals of data processing. In C. Tropea, A. L. Yarin, & J. F. Foss (Eds.), *Springer handbook of experimental fluid mechanics* (pp. 1399–1417). doi:10.1007/978-3-540-30299-5_23

Ol, M., McAuliffe, B., Hanff, E., Scholz, U., & Kaehler, C. (2005). Comparison of laminar separation bubble measurements on a low reynolds number airfoil in three facilities. In *35th aiaa fluid dynamics conference and exhibit.* doi:10.2514/6.2005-5149. eprint: https://arc.aiaa.org/doi/pdf/10.2514/6.2005-5149

Peng, D., & Gregory, J. W. (2015). Vortex dynamics during blade-vortex interactions. *Physics of Fluids, 27*(5), 053104. doi:10.1063/1.4921449

Pino Martín, M., Piomelli, U., & Candler, G. V. (2000). Subgrid-Scale Models for Compressible Large-Eddy Simulations. *Theoretical and Computational Fluid Dynamics*, *13*, 361–376.

Piomelli, U., Cabot, W. H., Moin, P., & Lee, S. (1991). Subgrid-scale backscatter in turbulent and transitional flows. *Physics of Fluids A: Fluid Dynamics*, *3*(7), 1766–1771. doi:10.1063/1.857956. eprint: https://doi.org/10.1063/1.857956

Piomelli, U., Zang, T. A., Speziale, C. G., & Hussaini, M. Y. (1990). On the large-eddy simulation of transitional wall-bounded flows. *Physics of Fluids A: Fluid Dynamics*, *2*(2), 257–265. doi:10.1063/1.857774. eprint: https://doi.org/10.1063/1.857774

Pope, S. B. (2000). *Turbulent flows.* doi:10.1017/CBO9780511840531

Qin, S., Koochesfahani, M., & Jaberi, F. (2018). Large eddy simulations of unsteady flows over a stationary airfoil. *Computers & Fluids*, *161*, 155–170. doi:https://doi.org/10.1016/j.compfluid.2017.11.014

Quadrio, M., & Luchini, P. (2003). Integral space–time scales in turbulent wall flows. *Physics of Fluids*, *15*(8), 2219–2227. doi:10.1063/1.1586273. eprint: https://doi.org/10.1063/1.1586273

Radespiel, R. E., Windte, J., & Scholz, U. (2007). Numerical and experimental flow analysis of moving airfoils with laminar separation bubbles. *AIAA Journal*, *45*(6), 1346–1356. doi:10.2514/1.25913. eprint: https://doi.org/10.2514/1.25913

Reed, W., & Hill, T. (1973). *Triangular mesh methods for the neutron transport equation.* Los Alamos Scientific Laboratory, Department of Energy, United States.

Restelli, M. (2017). Femilaro: A finite element toolkit. Retrieved from https://bitbucket.org/mrestelli/femilaro/wiki/Home

Restelli, M., & Giraldo, F. X. (2009). A conservative discontinuous galerkin semi-implicit formulation for the navier–stokes equations in nonhydrostatic mesoscale modeling. *SIAM Journal on Scientific Computing*, *31*(3), 2231–2257. doi:10.1137/070708470. eprint: https://doi.org/10.1137/070708470

Rival, D., Manejev, R., & Tropea, C. (2010). Measurement of parallel blade–vortex interaction at low reynolds numbers. *Experiments in Fluids*, *49*, 89–99. doi:10.1007/s00348-009-0796-1

Rockwell, D. (1998). Vortex-body interactions. *Annual Review of Fluid Mechanics*, *30*(1), 199–229. doi:10.1146/annurev.fluid.30.1.199. eprint: https://doi.org/10.1146/annurev.fluid.30.1.199

Saathoff, P. J., & Melbourne, W. H. (1997). Effects of free-stream turbulence on surface pressure fluctuations in a separation bubble. *Journal of Fluid Mechanics*, *337*, 1–24. doi:10.1017/S0022112096004594

Sagaut, P., & Meneveau, C. (2006). *Large eddy simulation for incompressible flows: An introduction.* Scientific Computation. Springer. Retrieved from https://books.google.it/books?id=ODYiH6RNyoQC

Sarlak, H. (2017). Large eddy simulation of an sd7003 airfoil: Effects of reynolds number and subgrid-scale modeling. *Journal of Physics: Conference Series*, *854*, 012040. doi:10.1088/1742-6596/854/1/012040

Selig, M. (1995). *Summary of low speed airfoil data.* Summary of Low Speed Airfoil Data. SoarTech Publications. Retrieved from https://books.google.it/books?id=qtIeAQAAIAAJ

Smagorinsky, J. (1963). General circulation experiments with the primitive equations: I. the basic experiment. *Monthly weather review, 91*(3), 99–164.

Steinhoff, J., & Raviprakash, G. (1995). Navier-stokes computation of blade-vortex interaction using vorticity confinement. In *33rd aerospace sciences meeting and exhibit.* doi:10.2514/6.1995-161. eprint: https://arc.aiaa.org/doi/pdf/10.2514/6.1995-161

Suwa, T., Nose, K., Numata, D., Nagai, H., & Asai, K. (2012). Compressibility effects on airfoil aerodynamics at low reynolds number. In *30th AIAA applied aerodynamics conference.* doi:10.2514/6.2012-3029. eprint: https://arc.aiaa.org/doi/pdf/10.2514/6.2012-3029

Tanabe, Y., Saito, S., Takasaki, K., & Fujita, H. (2009). A parametric study of parallel blade-vortex-interaction noise. *Noise Control Engineering Journal, 57.* doi:10.3397/1.3197849

Tanabe, Y., Saito, S., Yang, C., Aoyama, T., Benoit, C., Gretay, J., . . . Sides, J. (2007). *Inviscid numerical simulations of 2d parallel blade-vortex interaction JAXA/ONERA cooperation.* Japan Aerospace Exploration Agency (JAXA).

Tugnoli, M. (2017). *Polynomial adaptivity for large eddy simulation of compressible turbulent flows* (PhD Thesis, Politecnico di Milano).

Tugnoli, M., Abbà, A., & Bonaventura, L. (2019). Dynamical degree adaptivity for DG-LES models. In *Proceedings of the ICOSA-HOM 2018 conference.*

Tugnoli, M., Abbà, A., Bonaventura, L., & Restelli, M. (2016). A locally p-adaptive approach for large eddy simulation of compressible flows in a DG framework. *Journal of Computational Physics, 349.* doi:10.1016/j.jcp.2017.08.007

Uberoi, M. S. (1956). Effect of wind-tunnel contraction on free-stream turbulence. *Journal of the Aeronautical Sciences, 23*(8), 754–764. doi:10.2514/8.3651. eprint: https://doi.org/10.2514/8.3651

Uranga, A., Persson, P.-O., Drela, M., & Peraire, J. (2009). Implicit large eddy simulation of transitional flows over airfoils and wings. doi:10.2514/6.2009-4131

Vreman, B., Geurts, B., & Kuerten, H. (1995). Subgrid-modelling in LES of compressible flow. *Applied scientific research, 54*(3), 191–203.

Wang, L., Gobbert, M. K., & Yu, M. (2019). A dynamically load-balanced parallel p-adaptive implicit high-order flux reconstruction method for under-resolved turbulence simulation. arXiv: 1910.03693 `[physics.comp-ph]`

Wilder, M., & Telionis, D. (1998). Parallel blade–vortex interaction. *Journal of Fluids and Structures, 12*(7), 801–838. doi:https://doi.org/10.1006/jfls.1998.0172

Yoshizawa, A. (1986). Statistical theory for compressible turbulent shear flows, with the application to subgrid modeling. *PHYS. FLUIDS, 29*(7 , Jul. 1986), 2152–2164. cited By 361. doi:10.1063/1.865552

Zanotti, A., Ermacora, M., Campanardi, G., & Gibertini, G. (2014). Stereo particle image velocimetry measurements of perpendicular blade–vortex interaction over an oscillating airfoil. *Experiments in Fluids, 55.* doi:10.1007/s00348-014-1811-8

Zhang, W., Hain, R., & Kähler, C. J. (2008). Scanning piv investigation of the laminar separation bubble on a sd7003 airfoil. *Experiments in Fluids, 45*(4), 725–743. doi:10.1007/s00348-008-0563-8